Geophysical Prospecting

EAGE EUROPEAN ASSOCIATION OF GEOSCIENTISTS & ENGINEERS

Geophysical Prospecting, 2015, **63**, 1284–1310 doi: 10.1111/1365-2478.12278

Field test of sub-basalt hydrocarbon exploration with marine controlled source electromagnetic and magnetotelluric data

G. Michael Hoversten[1]*, David Myer[2], Kerry Key[1]†, David Alumbaugh[3], Oliver Hermann[4] and Randall Hobbet[4]

[1]*Chevron Energy Technology Company, 6001 Bollinger Canyon Road, K1010 San Ramon, CA 94583, USA,* [2]*Blue Green Geophysics,* [3]*Scripps Institution of Oceanography, and* [4]*Chevron Norge AS*

Received January 2014, revision accepted January 2015

ABSTRACT

The recent use of marine electromagnetic technology for exploration geophysics has primarily focused on applying the controlled source electromagnetic method for hydrocarbon mapping. However, this technology also has potential for structural mapping applications, particularly when the relative higher frequency controlled source electromagnetic data are combined with the lower frequencies of naturally occurring magnetotelluric data. This paper reports on an extensive test using data from 84 marine controlled source electromagnetic and magnetotelluric stations for imaging volcanic sections and underlying sediments on a 128-km-long profile. The profile extends across the trough between the Faroe and Shetland Islands in the North Sea. Here, we focus on how 2.5D inversion can best recover the volcanic and sedimentary sections. A synthetic test carried out with 3D anisotropic model responses shows that vertically transverse isotropy 2.5D inversion using controlled source electromagnetic and magnetotelluric data provides the most accurate prediction of the resistivity in both volcanic and sedimentary sections. We find the 2.5D inversion works well despite moderate 3D structure in the synthetic model. Triaxial inversion using the combination of controlled source electromagnetic and magnetotelluric data provided a constant resistivity contour that most closely matched the true base of the volcanic flows. For the field survey data, triaxial inversion of controlled source electromagnetic and magnetotelluric data provides the best overall tie to well logs with vertically transverse isotropy inversion of controlled source electromagnetic and magnetotelluric data a close second. Vertical transverse isotropy inversion of controlled source electromagnetic and magnetotelluric data provided the best interpreted base of the volcanic horizon when compared with our best seismic interpretation. The structural boundaries estimated by the 20-Ω·m contour of the vertical resistivity obtained by vertical transverse isotropy inversion of controlled source electromagnetic and magnetotelluric data gives a maximum geometric location error of 11% with a mean error of 1.2% compared with the interpreted base of the volcanic horizon. Both the model study and field data interpretation indicate that marine electromagnetic technology has the potential to discriminate between low-resistivity prospective siliciclastic sediments and higher resistivity non-prospective volcaniclastic sediments beneath the volcanic section.

Key words: Electromagnetic, Sub-basalt.

*E-mail: hovg@chevron.com
†Now at: NEOS Geosolutions

INTRODUCTION

Seismic imaging for hydrocarbon reservoirs located beneath basalt is often challenging due to the high velocity and extreme heterogeneity of basalt flows. When assessing the prospectivity beneath basalt, a critical factor is the presence of sediments within a depth range that will accommodate hydrocarbons. If sediments are present, the depth extent and structure of the overlying basalt is critical to constructing accurate velocity models for migration of seismic data and to develop drilling plans. Recent drilling results based on interpretation of the basalt thickness from seismic data on the Norwegian North Atlantic Margin (NAM) have shown misinterpretation of the basalt thickness in excess of 1 km in some cases. Exploration wells in the NAM cost in the range of hundreds of millions of U.S. dollars, so there is a significant motivation for using new technology to improve base basalt location. In this paper, we demonstrate that a combination of controlled source electromagnetic (CSEM) and marine magnetotelluric (MT) data can provide inversion models of the basalt section along with underlying sediment and structures that can be used to discriminate between differing seismic interpretations and hence reduce the risk for drilling predictions and improve migration velocity models.

Early application of marine MT data focused on imaging the base of resistive salt bodies (Constable *et al.* 2000; Hoversten, Morrison, and Constable 1998; Key, Constable, and Weiss 2006), whereas early application of MT and CSEM for imaging the base of basalt was first performed on land. Prieto *et al.* (1985), Warren and Srnka (1992), Withers *et al.* (1994), Morrison *et al.* (1996), and Smith *et al.* (1999) used MT data to image the base of massive basalt flows in the Columbia River Basin. More recently, Strack and Pandey (2007) and Colombo *et al.* (2011) have presented work using on-shore MT and CSEM for sub–basalt imaging and Jegen *et al.* (2009) combined gravity and MT data.

While there are a large number of exploration and production wells drilled on the NAM, relatively few have been drilled into basalt, and even fewer have penetrated the base. Only a few cases have been reported where marine CSEM and MT data were acquired over such well penetrations. In 2012, Chevron undertook a calibration survey of CSEM and MT data on a profile that spans the Faroe–Shetland Trough with the Faroe Islands to the northwest and the Shetland Islands to the southeast. This profile connected two wells that had penetrated the base of massive basalt flows: Brugdan to the northwest and Rosebank to the southeast. While the Rosebank well penetrated through basalt flows and underlying volcaniclastic into prospective siliciclastic sediments, the Brugdan well hit total depth in volcaniclastic sediments beneath the massive basalt flows. This test line was selected because we had two well penetrations of the volcanic section. Furthermore, the seismic definition of the base of the basalt was considered to be of high quality, at least around the Rosebank well. The quality of the seismic image of the base of the volcanic section is far worse in many other exploration plays.

SURVEY GEOMETRY AND DATA PROCESSING

The calibration survey is a combination of a 128-km-long regional 2D line with 86 CSEM/MT receivers connecting the two wells, and two small 12×12 km 3D surveys surrounding the Brugdan and Rosebank wells (Fig. 1). Of the 138 deployments planned for the survey, 135 returned usable CSEM data and 133 returned usable MT data, resulting in 84 successful stations along the 2D profile. The receiver spacing on the regional 2D line that ties the two wells is 1.5 km, whereas the receiver spacing of the orthogonal lines that make up the mini-3D surveys around the wells is 2 km. In this paper, we only consider the regional data from the 2D profile.

The survey spans the Faroe–Shetland Trough with receivers positioned at seafloor depths varying from 240 m to 1180 m (Fig. 2). Continuous measurements of water conductivity by the CSEM towfish, augmented by depth versus conductivity profiles measured using expendable bathythermographs, show the water conductivity varying from 3.70 S/m near the surface to 2.94 S/m at depth. To account for this variation, we built a stratified water model using the averaged conductivity in 100-m-thick layers extending to below the thermocline, where the water conductivity stabilizes.

Instruments were deployed using the standard free-fall technique and most landed within 100 m of their planned locations. Since no instrument carried a compass, instrument orientations were derived by post-processing the CSEM data. The contractor uses multiple, semi-independent methods whose details are held private as intellectual property. Therefore, we independently validated the reported orientations using the orthogonal Procrustes rotation method outlined in Key and Lockwood (2010). The differences between our solutions and the contractors have an approximately Gaussian distribution with a mean of zero and standard deviation of about 2°. Perturbation analysis shows that this level of orientation uncertainty corresponds to a relative uncertainty in the modelled CSEM and MT responses that is less than 1% for the inline receivers along the 2D profile.

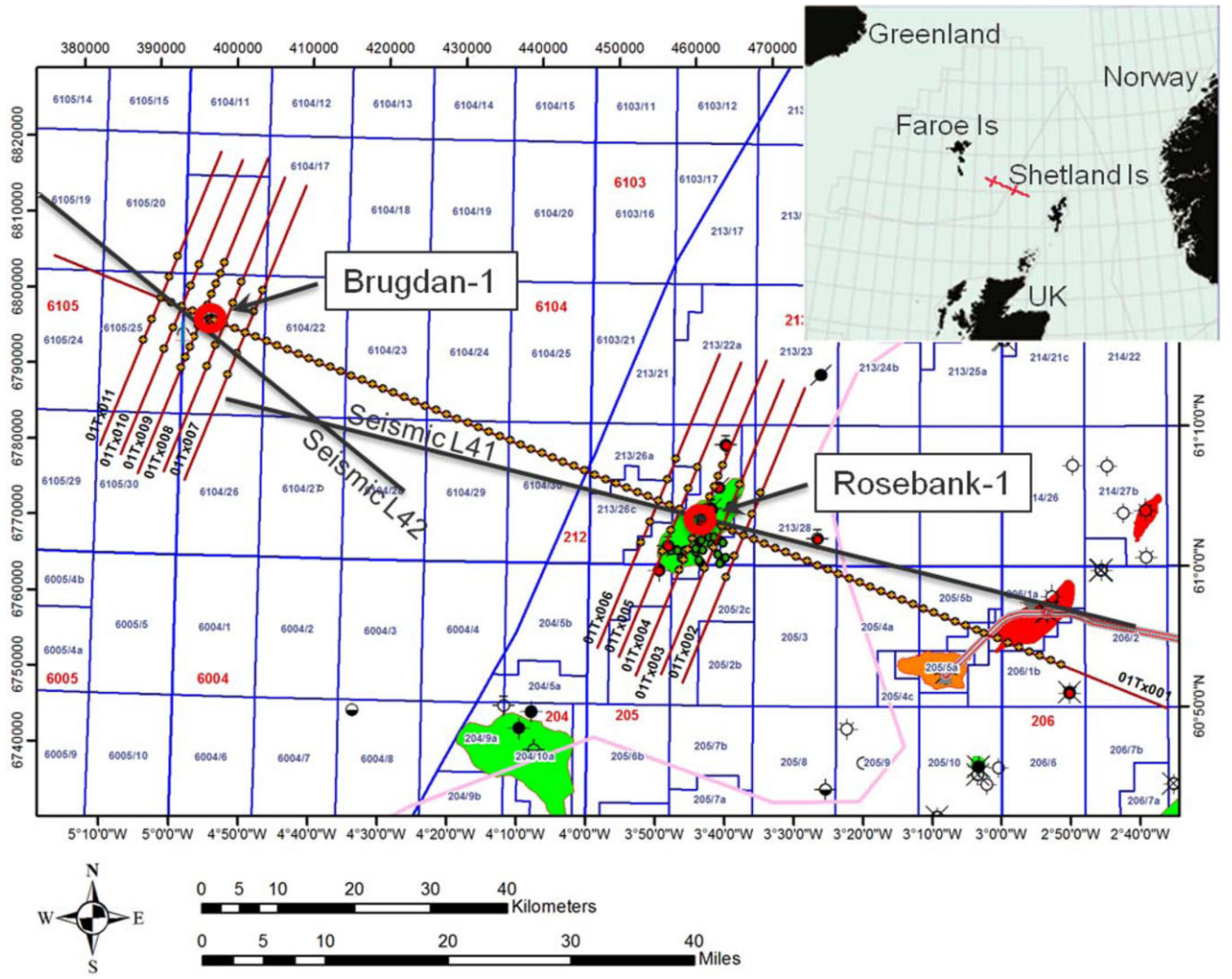

Figure 1 Base map showing the 2D regional CSEM/MT line with 1.5 km receiver spacing running from northwest to southeast over the Brugdan-1 and Rosebank-1 wells. Existing oil fields (green) and gas fields (red) are shown. Small 3D surveys are laid out around each well with 2-km receiver spacing on 5 towlines that are orthogonal to the 2D regional line.

MT impedance was derived using the robust, multivariate errors-in-variables method described by Egbert (1997), where data from multiple stations are used to discriminate coherent MT signal from incoherence noise. Because robust methods can sometimes return poor results if there are too many noise sources in the data (e.g., Weckmann, Magunia, and Ritter 2005), we used local coherence and amplitude measures to limit the input data to that with high-quality signal (i.e., retaining data with high coherence and omitting data with low amplitude). This greatly improved the quality of the resulting impedance.

The CSEM survey included eleven towlines, one across the Trough and five orthogonal tows over each 3D patch. In all, 395 receiver plus towline pairings were processed, and six frequencies were obtained: 0.2 Hz, 0.4 Hz, 0.6 Hz, 1.0 Hz, 1.4 Hz, and 2.6 Hz. CSEM transfer functions were derived by Fourier transform of the pre-whitened time series in waveform-length windows (5 s) and by robustly averaging to non-overlapping, 1-min windows using the method described by Myer, Constable, and Key (2011). This method has the advantage of providing an independent measure of noise for each estimate while reducing spectral contamination from lower frequency MT signal. Additionally, since data for each receiver are aligned in time, inversion of data from multiple receivers greatly reduces the number of unique transmitter positions required to be modelled as compared with data stacking that is based on the binning the data as a function of transmitter distance from each receiver.

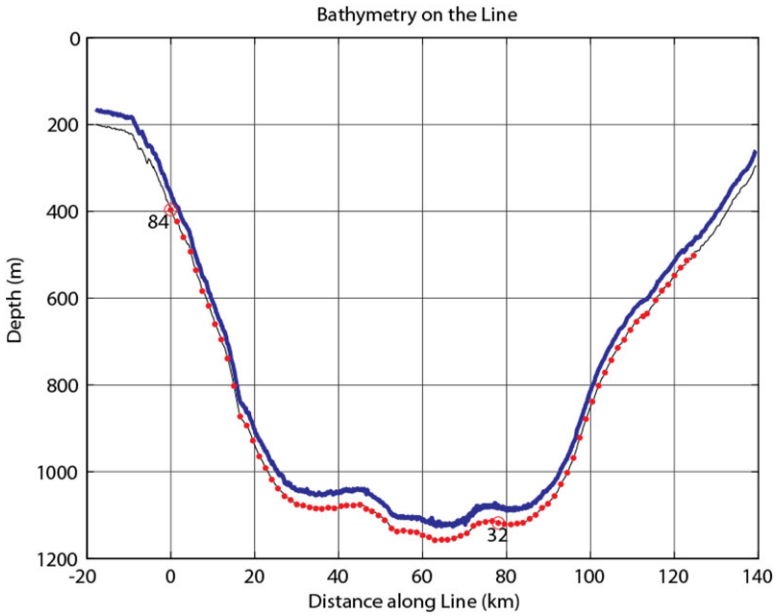

Figure 2 Bathymetry profile along the 2D regional line. Receivers are red dots, and the source positions are the blue dots. Distance along the line from receiver 84 (extreme northwest site) to receiver 1 (extreme southeast site) is shown in km. The locations of sites 32 and 84 whose data are displayed in Figs. 3–5 are highlighted.

The processed data exhibit a moderate amount of spatially correlated noise in the sites spanning the deepest parts of the trough, which we suspect is due to bottom currents creating electromagnetic noise through a combination instrument shaking and possibly localized motional induction. Figure 3 shows the CSEM data for a shallow water station and a deep-water station, where only data with a signal-to-noise ratio (SNR) greater than or equal to 3 are displayed. The increased noise in the trough results in significantly reduced range for the deeper site. Figure 4 shows the MT data at the same two sites, where the effect of increased signal attenuation by the water column can be seen in the slightly increased variability of the response at the shortest periods for the deep water site (32) compared with the shallow water site (84). Here the variability caused by low signal levels exceeds the estimated error from the MT procession code. For this reason, we set a 10% minimum uncertainty on the MT responses.

Examination of the MT polar diagrams shows that at periods less than 85 s, the MT data are essentially 1D without any significant differences between the Z_{xy} and Z_{yx} impedance variables. The polar diagrams show that, at long periods, the geo-electric strike averages 135° east of north, whereas the line orientation is 112° east of north.

For the CSEM data, the error structure includes the effects of both random noise and position uncertainties. The random noise is derived from the independent data stacking estimates calculated during processing and an absolute noise floor picked for each channel and frequency based on selecting the amplitude where the point-to-point coherence breaks down. Position uncertainties are calculated based on perturbation analysis of uncertainties in the transmitter and receiver positions and orientations as described by Myer *et al.* (2011). These two independent sources of uncertainty are added in quadrature, and the final error structure is subject to a 2% minimum error. CSEM data were also trimmed to source–receiver offsets between 1 km and 20 km and SNRs greater than 3 (except in the trough where a cutoff value of 4 was used because of the higher noise environment). The resulting data typically extend to a 15-km range in the shallow water and 10 km in the deep.

BASALT RESISTIVITY

Examination of available logs that have penetrated basalt shows a wide range of basalt resistivity, ranging from tens to thousands of ohm-metres. In addition to the wide resistivity range, the basalt can vary from massive uniform flows to highly interbedded flows and sediments. The presence of interbedding can produce large-scale resistivity anisotropy. In addition to the transverse vertical anisotropy caused by interbedding, flows can be faulted in such a way that could produce triaxial resistivity anisotropy. The two wells on the calibration line (Brugdan and Rosebank) were used to calculate large-scale horizontal and vertical resistivity using the series and parallel circuit analogy. An averaging interval of 100 m was used to calculate the average conductance and

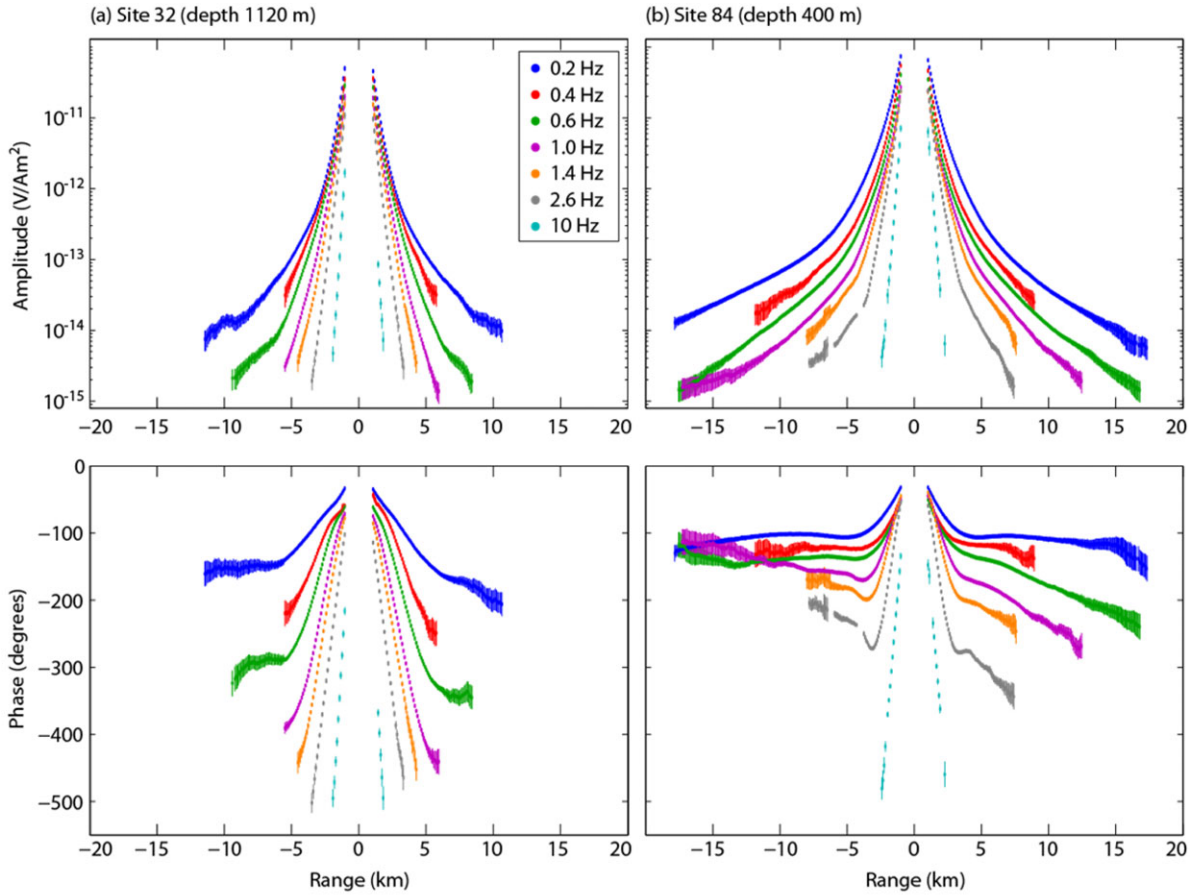

Figure 3 Representative CSEM data shown for sites 32 (a) and 84 (b). Upper panels show the in-line electric field amplitude per unit transmitter moment. Lower panels show the phase in degrees. Only data with SNRs greater than or equal to three are shown.

resistance, which suggest vertical to horizontal anisotropy ratios exceeding ten.

QUANTIFYING THE INVERSION RESULTS

Picking the base of the volcanic section from regularized inversion requires using some property of the inverted resistivity structure as a proxy for the base. We have considered calculating the gradient of the resistivity and finding the maximum vertical or total gradient, as well as picking a resistivity contour from the inverted resistivity. We have found that the gradient calculations are less accurate than using a resistivity contour that provides a best fit to the base from model studies. For the inversion of synthetic data to follow, we define the relative error E_i between a chosen contour and the true base volcanics as given by:

$$E_i = \left(\frac{Ib_i - Tb_i}{Tb_i} \right) 100, \quad (1)$$

where Ib_i is the depth of the chosen contour, and Tb_i is the true base depth at position i. In addition, the mean of the absolute value of all E_i along the base is calculated to provide a mean absolute value percentage error. For the inversions of field data, Tb_i is replaced with the seismic pick for base volcanics.

In order to quantify the ability of the inversions to reconstruct the resistivity, we extracted vertical profiles at three locations, representing thin to thick volcanic sections. The locations of the vertical profiles at 12, 24, and 30 km along the line are shown on all the model inversion figures. The base of the volcanic section (flows and volcaniclastic) at each location was used to separate the profiles into volcanics and sediments for calculation of the relative difference between inversion and true resistivity. This was done for MT and CSEM isotropic inversions, as well as for vertical transverse anisotropy (VTI) and triaxial anisotropy inversions of both the CSEM data and the joint CSEM and MT data.

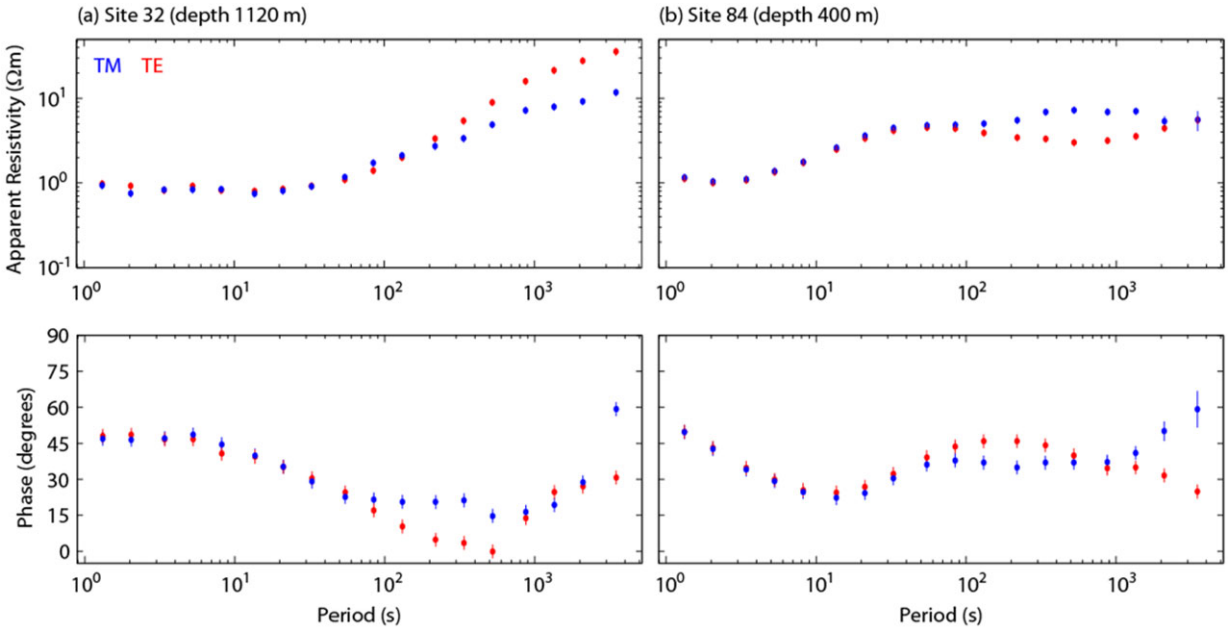

Figure 4 Representative MT apparent resistivity and phase data at sites 32 (a) and 84 (b). The TM mode is defined as the impedance tensor component corresponding to the electric field in the line direction with the horizontal magnetic field orthogonal to the line direction. The TE mode corresponds to the horizontal electric field orthogonal to the line direction with the magnetic field along the line direction.

A number of ways of characterizing the fidelity of the inversion in the basalt and underlying sediments were considered. We found that calculating the vertical integrated resistance (VIR) within the resistive volcanic section (between top and base horizons) and the vertical integrated conductance (VIC) within the conductive sediment section (between base volcanics and top basement at 5 km depth) produced the best representation of the quality of the inversion. The percent difference in VIR between inversion and model in the volcanic section R_{diff} is given in equation (2) below and shown in the upper half of Table 1. The percentage difference in the VIC in the sediment section C_{diff} is given by equation (3) below and shown in the bottom half of Table 1. We will discuss the interpretation of Table 1 as we consider the different inversions.

$$R_{diff} = \left(\left(\sum_{i=1}^{N} \rho_i^{True} T_i - \sum_{i=1}^{N} \rho_i^{Inv} T_i \right) \Big/ \sum_{i=1}^{N} \rho_i^{True} T_i \right) 100 \quad (2)$$

$$C_{diff} = \left(\left(\sum_{i=1}^{N} \sigma_i^{True} T_i - \sum_{i=1}^{N} \sigma_i^{Inv} T_i \right) \Big/ \sum_{i=1}^{N} \sigma_i^{True} T_i \right) 100 \quad (3)$$

where ρ_i^{True} and σ_i^{True} are the true resistivity and conductivity, respectively, of the ith cell in the resistive and conductive sections, T_i is the thickness of the ith cell, and ρ_i^{Inv} and σ_i^{Inv} are the inversion resistivity and conductivity, respectively, of the ith cell in the resistive and conductive sections.

FEASIBILITY STUDY

A fine-scale 3D numerical model of a sub–basalt prospect on trend with our calibration line was constructed to investigate the resolution and accuracy of CSEM/MT imaging techniques. The 3D model was constructed using regional well-log, seismic, and geologic data to create a porosity and saturation volume from which geophysical properties such as velocity, density, and electrical resistivity could be calculated using regression relationships derived at nearby wells. Different relationships were derived for the siliciclastic sediments and three volcanic lithology types: volcanic flows, volcaniclastic sediments, and hyaloclastites. The model was discretized at a 6-m cell size for the seismic finite-difference modelling and upscaled to 25-m cells for the CSEM and MT modelling (Alumbaugh *et al.* 2013).

We did not have access to three-component resistivity logs in basalt. However, macro-scale parallel and series circuit analogy of existing induction log resistivity profiles suggest that the large-scale vertical-to-horizontal resistivity anisotropy can sometimes exceed ten in the highly layered volcanic flows. For comparison, sediment transverse anisotropy

Table 1 Percentage difference in the VIR between top and base volcanics (upper section) and percentage difference in VIC between base volcanics and basement at 5-km depth (lower section) at 12 km, 24 km, and 30 km easting along the line shown in Fig. 5. Positive resistance means the inversion has too much resistivity, and positive conductance means the inversion has too little resistivity (or too much conductivity). These sites are representative of the different volcanic thicknesses along the line. For isotropic inversion, the inverted resistivity is compared with all three resistivity values in the model. For VTI inversions, the VIR and VIC of the horizontal resistivity is compared with the VIR and VIC of the X and Y model resistivity, and the VIR of the inverted vertical resistivity is compared with the VIR of the model vertical resistivity. The percentage error is color coded so that hot colors are negative error and cool colors are positive error. The average of the absolute values of the percentage errors is given in the final row of each section in green. The absolute value eliminates the cancellation of equal but opposite errors. Overall, VTI inversion produces the lowest errors over both the resistive and conductive sections.

% Error in Vertical Integrated Resistance (VIR)							
Location	Component	CSEM Only			CSEM & MT			MT
		Isotropic	VTI	Triaxial	Isotropic	VTI	Triaxial	Isotropic
12km Volcanics (700 m)	ρ_x	214	-45	-19	162	-53	-13	-84
	ρ_y	214	-45	-29	162	-53	-27	-84
	ρ_z	26	1	1	5	2	-3	-93
24km Volcanics (1000 m)	ρ_x	445	61	5	427	-55	2	-65
	ρ_y	952	210	105	918	-13	103	-38
	ρ_z	11	6	-56	7	-6	-1	-93
30km Volcanics (2400 m)	ρ_x	119	4	17	138	-46	11	-91
	ρ_y	330	104	114	370	6	106	-82
	ρ_z	-55	-56	-56	-52	-59	-55	-98
Average Abs. Values		263	59	45	249	33	36	81

% Error in Vertical Integrated Conductance (VIC)							
Location	Component	CSEM Only			CSEM & MT			MT
		Isotropic	VTI	Triaxial	Isotropic	VTI	Triaxial	Isotropic
12km Sediments (700 m)	ρ_x	-7	-7	-36	-18	-13	-36	-50
	ρ_y	-7	-7	-13	-18	-13	-13	-50
	ρ_z	126	-16	13	97	19	22	21
24km Sediments (1000 m)	ρ_x	18	9	-78	34	6	-4	-32
	ρ_y	18	9	-64	34	6	-1	-32
	ρ_z	188	46	-44	225	32	70	66
30km Sediments (2400 m)	ρ_x	-19	-6	-37	-26	-4	-25	36
	ρ_y	-19	-6	-6	-26	-4	-2	36
	ρ_z	85	14	53	69	80	69	211
Average Abs. Values		54	13	38	61	20	27	59

values of two to three are common and can sometimes reach a factor of ten or more (Klein *et al.* 2007; Ellis and MacGregor 2012; Colombo *et al.* 2013).

The assumed coordinate system for the 3D synthetic model has the *x*-direction in the in-line direction and the *y*-direction in the strike direction. Transverse anisotropy is assumed in the sediments, hyaloclastites, and volcaniclastics with vertical resistivity being 2.5 times larger than the horizontal resistivity. Because the volcanic flows have a high degree of spatial variability in addition to rift-faulting parallel to strike, the flows are assumed to exhibit triaxial anisotropy. The vertical resistivity is five times that of the resistivity perpendicular to strike (*x*-direction), and the resistivity parallel to strike (*y*-direction) is half that of the perpendicular resistivity (*x*-direction). The basement has transverse anisotropy with the vertical resistivity two times the horizontal resistivity. Figure 5 shows depth sections of the triaxial resistivity through the long axis of the model. The sections are parallel to the simulated CSEM acquisition lines. The acquisition lines run approximately 75° from the average geologic strike of the 3D model. Ideally, CSEM and MT lines would be run orthogonal (90°) to geo-electric strike, but the angle of 75° was chosen to allow for inaccuracy in survey design when the actual geo-electric strike is unknown.

The synthetic data were generated using the 3D finite-difference algorithm of Commer and Newman (2009). The full MT impedance tensor was calculated at five frequencies per decade from 3×10^{-4} Hz to 0.63 Hz, for a total of 17 frequencies. The CSEM simulations were computed for five frequencies (0.125 Hz, 0.25 Hz, 0.5 Hz, 1 Hz and 2 Hz) using reciprocal sources oriented in the x- and y-directions located at the true receiver positions, and electric fields computed at the true source positions in the direction of the towline. For the MT synthetics, 5% random Gaussian noise was added to both apparent resistivity and phase. The synthetic CSEM data were contaminated with 2% Gaussian noise for both the in-phase and out-of-phase components, and a 10^{-15} V/m noise floor was assumed. In the following discussion, the data from the line shown in Fig. 5 will be referred to as the data on "the line."

Analysis of the 3D synthetic data showed that there was between 2% and 5% numerical noise on the MT and CSEM data, which we ascertained by comparison between 2D finite-element and 3D finite-difference model responses for a 2D model. Because the 2D FE code uses automated adaptive mesh refinement with demonstrated accuracy to 1% (Key and Ovall 2011), deviation from the 2D response from the 3D code is deemed to be an error in the 3D code arising from the model grid cell size. Thus, the total noise in the simulated 3D data is greater than the added Gaussian noise. This meant that some inversions of synthetic 3D data were fitting numerical noise when the root-mean-square (RMS) misfit was driven to 1 with the assumed errors equal to the added noise. Just as with field data where the true error may not be captured in the estimated data errors, we use L-curve analysis for each inversion of synthetic data, choosing the iteration just past the major break in RMS versus roughness. It must be noted that there is a subjective element to picking the optimal iteration after the corner in the L curve. Past the corner in the L curve, the inversion models exhibit increased internal structure due to over fitting of the data. An interpretation has to be made as to how much structure is geologic and how much is spurious due to fitting data noise. Our interpretative use of the L curve resulted in RMS data misfits between 1 and 1.5 for all CSEM and MT inversions.

We use the 2.5D inversion code developed at Scripps Institution of Oceanography (Key and Ovall 2010; Key 2012) to test its spatial and resistivity resolution on a 3D synthetic model data set using various combinations of data: MT only, CSEM only, and joint CSEM and MT data. Joint inversion for MT and CSEM data simply means, at least in our implementation, that the data array contains both MT and CSEM data. Therefore, it is essentially the same inversion methodology as solo inversion. The inversion fits the $\log_{10}$ of MT apparent resistivity, the $\log_{10}$ of electric field amplitude of CSEM data, and the unwrapped phases in degrees. The model resistivity values are always bounded between 0.5 Ω·m and 1000 Ω·m using a non-linear parameter transformation (Key 2012). All the MT inversions presented here used both transverse electric (TE) and transverse magnetic (TM) mode data. The model roughness penalty was set to use a horizontal to vertical smoothing factor of 3:1 in order to encourage the inversion to prefer horizontal layering in the model. In the anisotropic inversions, an additional regularization penalty term against anisotropy was introduced with the objective of restricting anisotropy to only where it is required by the data. Through trial and error testing, we found that weighting the anisotropy penalty with a weight of 0.3 relative to the spatial roughness penalty worked well. The starting model for all of the inversions of synthetic 3D data was 2 Ω·m above the top basalt and 100 Ω·m below the top of basalt. For our synthetic tests, we assumed the top of the basalt was well constrained by seismic data; hence, we relaxed the inversion's roughness penalty across this known boundary. While the finite-element meshes extend to 100 km in all directions to satisfy boundary conditions, only the region from –5 km to 35 km and 0 km to

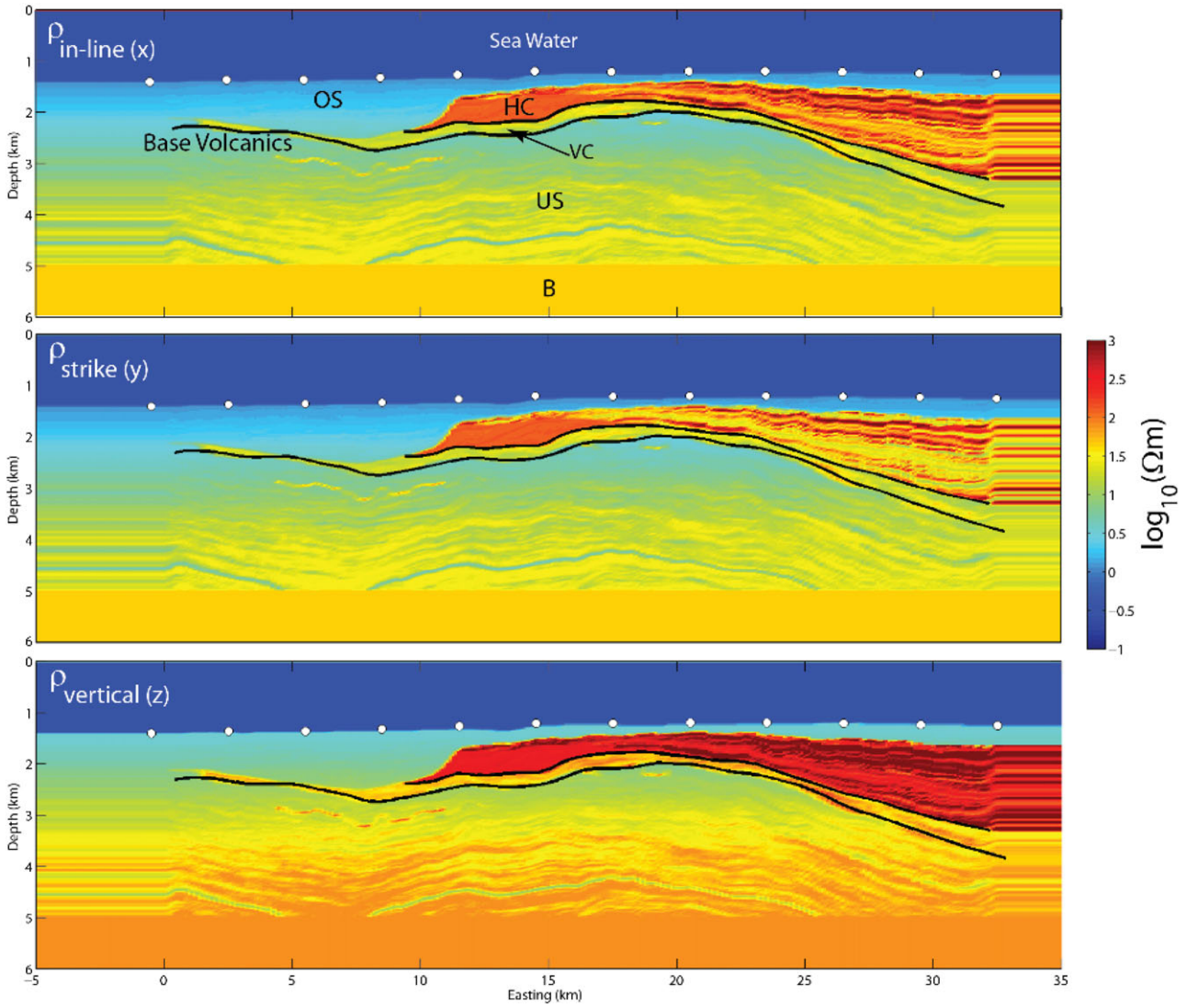

Figure 5 Resistivity depth sections along the long axis of the triaxial resistivity model. Sections are ~75° off from the average geologic strike of the model. Model units are overburden sediments (OS), hyaloclastic (HC), volcaniclastic (VC), volcanic flows (VF), underburden sediments (US), and basement (B). Transverse anisotropy is assumed in the sediments, hyaloclastites, and volcaniclastics with vertical resistivity being 2.5 times larger than the horizontal resistivity. Because the volcanic flows have a high degree of spatial variability in addition to rift-faulting parallel to strike, the flows are assumed to exhibit triaxial anisotropy. The vertical resistivity (z) is five times that of the resistivity in the in-line direction (x) and the resistivity parallel to strike (y) is half that of the in-line resistivity. The basement has transverse anisotropy with the vertical resistivity twice the horizontal resistivity.

6 km in *X* and *Z*, respectively, are shown, with the exception of the MT only inversion that extends to 30 km in *Z* to show deep structure.

As discussed, we found that using a resistivity contour as a proxy for the base of the volcanic section was the best way to provide an interpreted base volcanic from the regularized inversions. For the synthetic model, the 40-Ω·m contour was found to be close to optimal for all inversions and thus is displayed on all inversions for comparison.

Figure 6 shows the MT isotropic inversion along the line, where the data were fit to RMS of 1.5. The inversion indicates the presence of the high–resistivity volcanic section; however, the resolution is poor. The lack of resolution of the resistive volcanic section by the MT data is primarily due to the lower resolution of MT data for resistors compared with conductors, as well as the lack of frequencies above 1 Hz. Figure 7 shows the synthetic and inverse model data for the 17 frequencies and 12 receiver positions along the line. Note

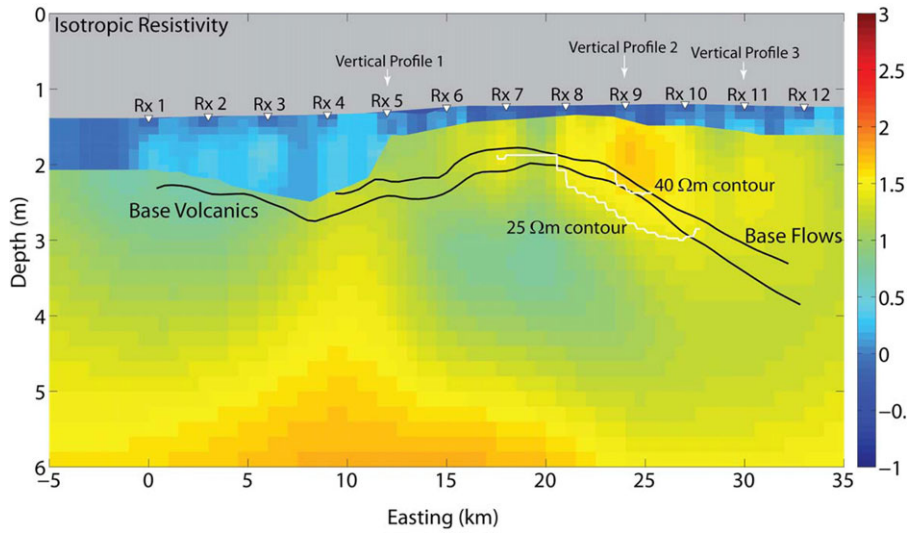

Figure 6 2D inversion of the synthetic model MT data at frequencies from 0.65 Hz to 0.003 Hz. The starting model was 2 Ω·m from the seafloor to top of the volcanics and 100 Ω·m below the top volcanics. Base flows and base volcanics from the synthetic model are shown as black lines. The 25- and 40-Ω·m contours from the inversion are shown as white lines for reference. Relative error calculations between the synthetic and inverse models at vertical profiles 1, 2, and 3 are given in Table 1.

that the apparent resistivity for both modes at the highest frequency of 0.63 Hz only exceeds 2 Ω·m at sites 6–9, where the sediment overburden is thinnest, reaching a maximum of 4 Ω·m at 0.63 Hz at site 8. The apparent resistivity response indicates a very limited sensitivity to the shallow high resistive volcanics, as is evidenced by the inversion result in Fig. 6.

Figure 8 shows the isotropic inversion of only the CSEM data along the line. The base of the high-resistivity flows is marked "base flows" and the base of the volcaniclastic section is marked "base volcanic." In addition, the resistivity contour that most closely matches the base of the volcanic section is the 40-Ω·m contour that is marked as the white line. The maximum error (see equation (1)), between the 40-Ω·m contour and the base of the volcanic section is +14% with a mean absolute value error of 5.3%. A visual comparison between the isotropic inversion of Fig. 8 and the model sections of Fig. 5 shows that the isotropic resistivity most closely resembles the vertical resistivity in the volcanic section and the horizontal resistivity in the sedimentary section beneath. The general structure of the volcanic section is well recovered, with indication of the less resistive volcaniclastic sediments that lie beneath the flows and extend to the left between 0 km and 10 km. The almost layered artefact structure in the conductive overburden is associated with isotropic inversion of anisotropic data. The deeper increase in resistivity to 80 Ω·m at 5-km depth is blurred with a "pull up" in the anticline under the volcanics where the thickest section of conductive sediments lies.

Figure 9 shows the vertical profiles at 12 km, 24 km, and 30 km extracted from the model shown in Fig. 8. The isotropic inversion is shown as the solid red line with the true anisotropic model in-line (x), strike (y), and vertical (z) resistivity values shown as the dashed red, green, and black lines, respectively. Examination of Fig. 9 shows that the isotropic inverse resistivity is closest to the vertical resistivity in the high resistivity volcanic flows and closest to the lower of the two horizontal resistivities (the strike direction) below the volcanic flows. These observations are borne out in the VIR and VIC errors in the volcanic and sedimentary sections, respectively, shown in Table 1.

Figure 10 shows the horizontal resistivity and the vertical resistivity from the VTI inversion of the CSEM–only data along the line. The base of flows and volcanics as well as the 40-Ω·m contour are shown as before. In this example, the maximum relative error between the 40-Ω·m contour and the base of the volcanic section is –17% with a mean absolute value error of 7.5%. Comparing the VTI inversion of Fig. 10 with the isotropic inversions of Fig. 8, three major differences stand out. First, the layered artefacts in the overburden sediments are gone in the VTI inversion. Second, the conductive sediments beneath the volcanics are mainly expressed in the horizontal resistivity with only a slight indication of the decrease in resistivity shown in the vertical resistivity. Third, the deep resistivity structure caused by the transition from sediment to the resistive basement at 5 km is far less extreme in the VTI inversion. The flat basement resistor at 5-km depth

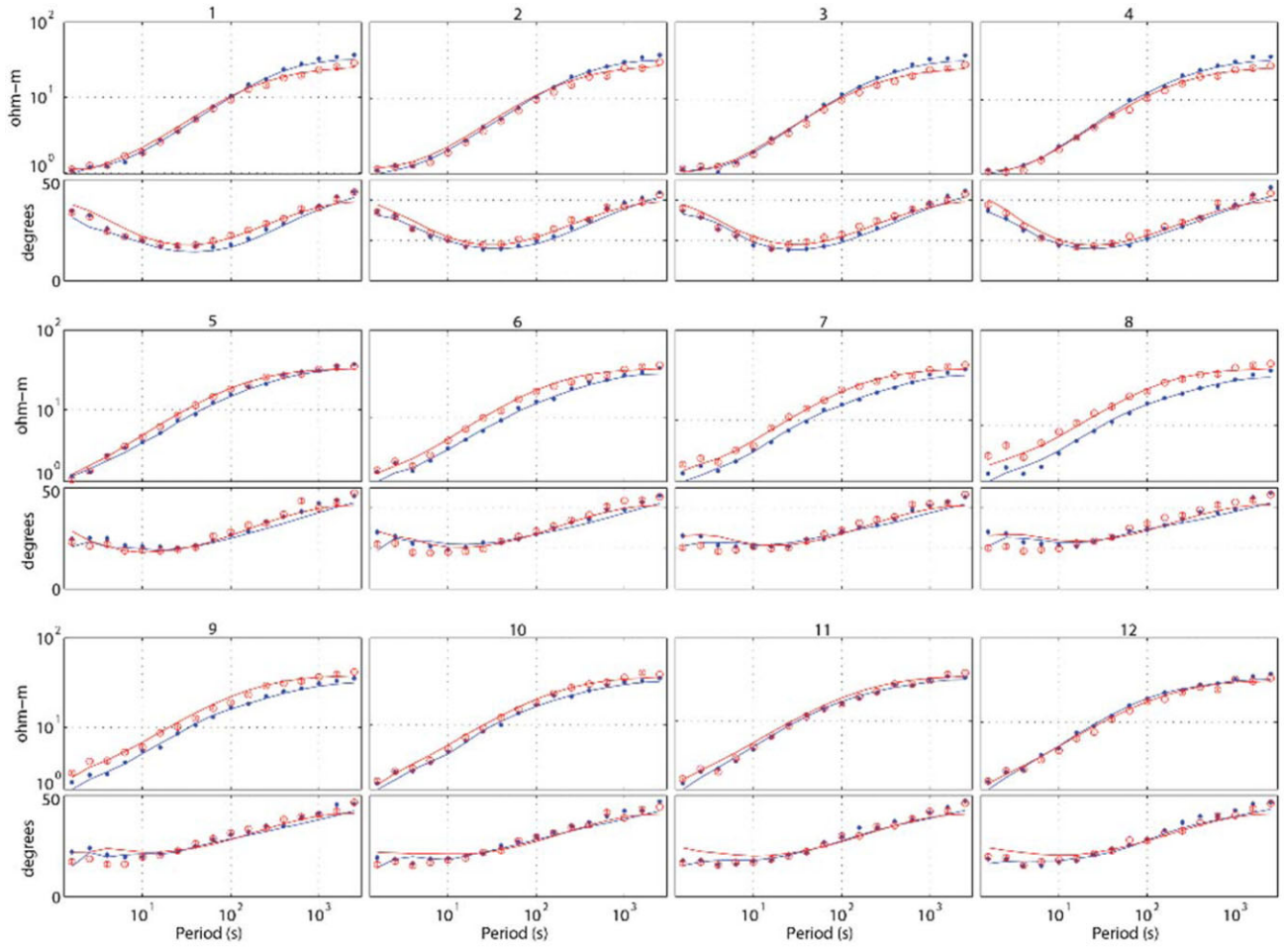

Figure 7 Synthetic MT apparent resistivity and phase (symbols) and calculated apparent resistivity and phase for sites 1–12 from the inverse model shown in Fig. 6 (lines). Red symbols and lines show the TE data, and blue symbols and lines show the TM data.

is still not well recovered beneath the thickest sub-volcanic sediment section at around 30-km position.

The high resistivity profile of the volcanics is well resolved, with the vertical resistivity closely matching the model, as was the case with the isotropic inversion of Fig. 8. In the volcanics, the inversion horizontal resistivity is over–estimated compared with the model. However, in the sub–volcanic sediments, the horizontal resistivity is closer to the model than the vertical resistivity. The inversion vertical resistivity in the sediments is consistently low compared with the model resistivity.

Figure 11 shows the triaxial anisotropy inversion using both the CSEM and MT data. The 40-Ω·m contour of the vertical resistivity is shown in white. The maximum error between the 40-Ω·m contour and the base of the volcanic section is –13%, with a mean absolute value error of 4%.

The major improvement compared to the CSEM–only VTI inversion of Fig. 10 is in the sub-volcanic sediments and the basement resistivity at 5 km. Visually, the deep in-line (x) and strike (y) resistivity shown in Fig. 11 is flatter with less of the depression in the deep resistivity under the thickest part of the sub-volcanic sediments, around 20-km horizontal position. The improvements in the sediment resistivity are harder to see from the displays but become apparent when considering the sediment VIC errors shown in Table 1.

Table 1 illustrates some important points about the inverse model resolution in the resistive and conductive sections. In the resistive volcanic section for volcanic thickness of 700 m and 1000 m, the ρ_z VIR is well determined by all data-type inversions, with VTI and triaxial performing the best. As the volcanic section thickens to 2400 m, all the inversions underestimate the ρ_z VIR by at least 50%. Adding MT to the isotropic inversion improves the ρ_z VIR particularly at thickness of 700 m and 1000 m. With a few exceptions, the ρ_y VIR is always the least accurately recovered. This is not surprising

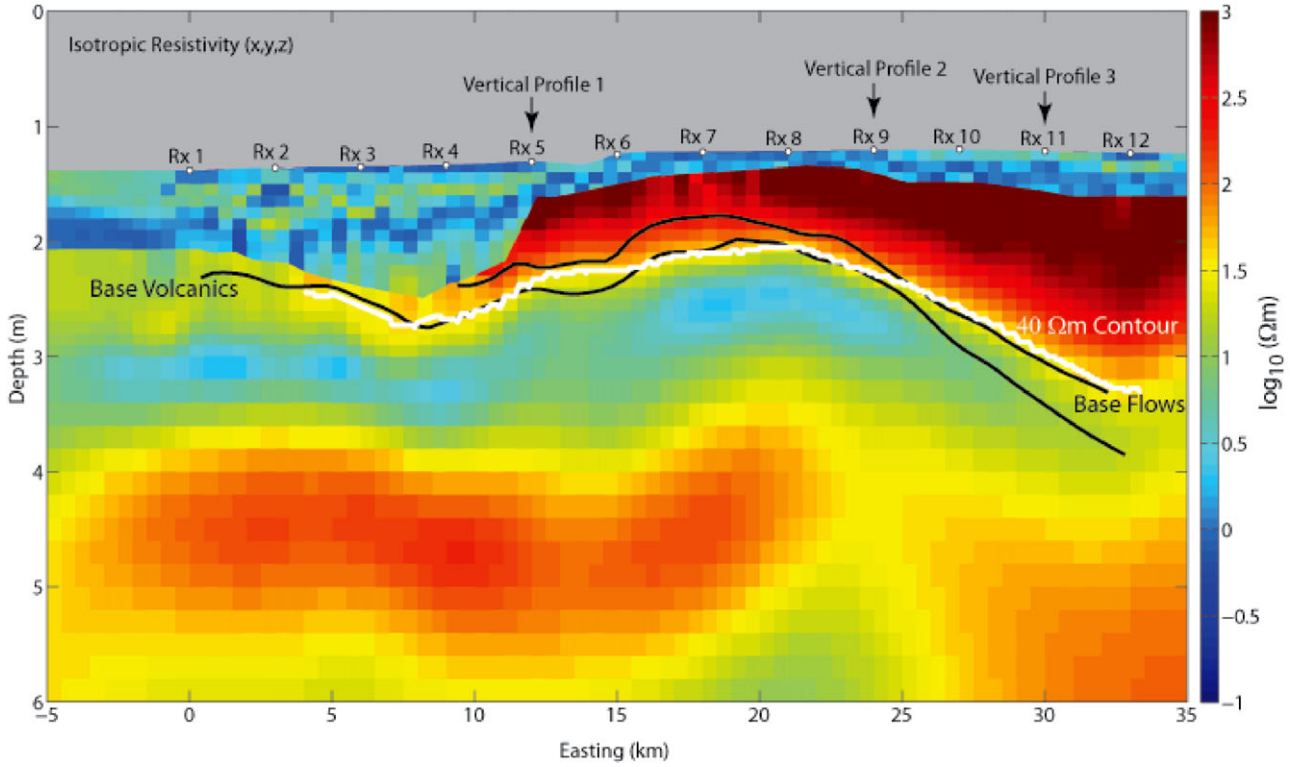

Figure 8 Isotropic inversion of CSEM only data. The starting model was 2 Ω·m from the seafloor to top of the volcanics and 100 Ω·m below the top volcanics. The base of the volcanics and base of the high resistivity flows are marked with the black line. The 40-Ω·m contour from the inversion is shown by the white line. Positions of three vertical resistivity profiles shown in Fig. 9 are shown. The relative error calculations between the synthetic model and inverse model at these locations are given in Table 1.

given that our inversions are only using inline CSEM data where currents are predominantly in the vertical xz plane and hence have minimal sensitivity to the across line resistivity ρ_y. Although one might expect the addition of TE mode MT data would improve this situation, the triaxial inversion results for ρ_y from inverting both CSEM and MT data show no significant improvement over the CSEM only inversion. When considering the average of the absolute value of the errors, the VTI and triaxial VIR estimates for both CSEM only and CSEM and MT data are close to each other compared with the isotropic and MT only values, with the best average estimates coming for triaxial using CSEM and MT data.

Considering the conductive section between the base of volcanics and the basement at 5-km depth, typically, the horizontal (ρ_x and ρ_y) VIC estimates are better than the VIC from the vertical resistivity. The average of the absolute value of the errors is slightly better for the CSEM-only VTI inversion compared with the CSEM and MT data VTI inversion. However, the CSEM and MT VTI average absolute values are skewed by the large ρ_z VIC error for the 3-km-thick section. If we consider only the VIC estimates from the horizontal resistivity, the CSEM and MT VTI inversion produces a lower average of the absolute values of the errors.

Three general statements can be made from Table 1: (i) Overall triaxial inversion produces the best ρ_z VIR estimates in the resistive volcanic section; (ii) VTI inversion produces the best horizontal VIC estimates in the conductive section beneath the volcanics; (iii) the average of the absolute value of VIC errors for the less-resistive sedimentary section are lower for all inversions compared with the average of the absolute value of the VIR errors of the more resistive volcanic section. This is consistent with the physics whereby the impressed and induced current density, and hence response, is much higher in the conductive sediments compared with the resistive volcanic section.

In the examples shown in Figs. 8, 10, and 11 we have plotted the 40-Ω·m contour. While each inversion could have its own optimal contour to match the base volcanics, the 40-Ω·m contour is very close to optimal for all three and illustrates an important point. Figure 12(a) shows the true base volcanics

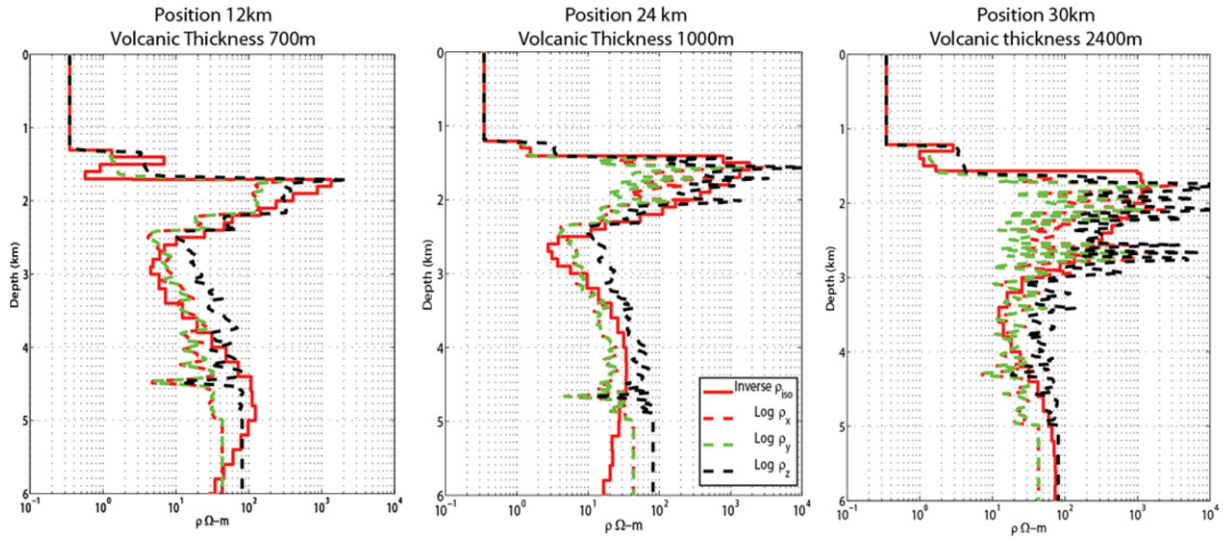

Figure 9 Vertical profiles of isotropic resistivity from CSEM-only inversion shown in Fig. 8. The inversion resistivity is solid red line, the synthetic model in-line (x), strike (y), and vertical (z) resistivity are shows as the dashed red, green, and black lines, respectively. The location of the profiles is marked on Fig. 8 as vertical profiles 1, 2, and 3.

depth with the depths of the 40-Ω·m contour for the inversions shown in Figs. 8, 10, and 11. Figure 12(b) shows the percentage error as defined by equation (1). Over the entire depth range of the base of the volcanic section, the 40-Ω·m contour of the vertical resistivity from the triaxial inversion of the joint data set (Fig. 11) is the closest to the true base. For both the isotropic (Fig. 8) and VTI (Fig. 10) inversions, the 40-Ω·m contour (or any contour) does not fit the true base over the entire depth range. The isotropic inversion produces the best match to the true base depths when the volcanic section is thin. The MT-only inversion shown in Fig. 7 is by far the worst, not having a constant contour to pick over much of the base. This suggests that the choice of data and contour to use for base volcanic interpretation will be situation dependent and should be guided by model studies for particular cases.

FIELD DATA INVERSION RESULTS

When considering the inversions of the field data shown here, it is important to keep in mind our two main objectives: to be able to accurately map the base of the high resistivity–velocity volcanic section and to accurately determine the resistivity of the underlying sediments. Accurately predicting the base of the high-velocity volcanic sections is needed to determine if underlying sediments lie within the hydrocarbon play window. Accurately predicting the resistivity of the underlying sediments is needed to assess if those sediments are non-prospective volcaniclastics or prospective siliciclastic sediments.

In this section, we consider five separate inversions: (i) an isotropic model with MT data only, (ii) an isotropic model with CSEM data only, (iii) a VTI model with CSEM data only, (iv) a VTI model using both CSEM and MT data, and (v) a triaxial resistivity model using both CSEM and MT data. In order to quantify the inversion predictions of basalt resistance, sub-basalt sediment conductance, and sub-basalt sediment horizontal resistivity at the wells, we use the depth intervals defined by the log interpretations. The basalt section at the Rosebank well lies between 2572 m and 2911 m and at Brugdan between 1173 m and 3175 m. The sub-basalt sediment section at Rosebank is classified as siliciclastic and lies between 2911 m and 3400 m. At Brugdan, the sediment section is classified as volcaniclastic and lies between 3175 m and 3745 m. Table 2 lists the percentage error in section resistance and conductance as defined by equations (2) and (3). In addition, because we are interested in distinguishing siliciclastic from volcaniclastic sediments in the sub-basalt sections, we list the log-averaged horizontal resistivity, the inversion horizontal resistivity averaged over the same intervals, and the percentage errors. The percentage error in the resistivity is defines as ((log-inversion)/log)*100; hence, a positive value means the log value is greater, and a negative value means the inversion value is greater. The MT inversion is not considered due to its poor to non-existent basalt section definition.

Before making some observations about the results in Table 2, it must be remembered that the induction logs only measure the horizontal resistivity within a few metres of a

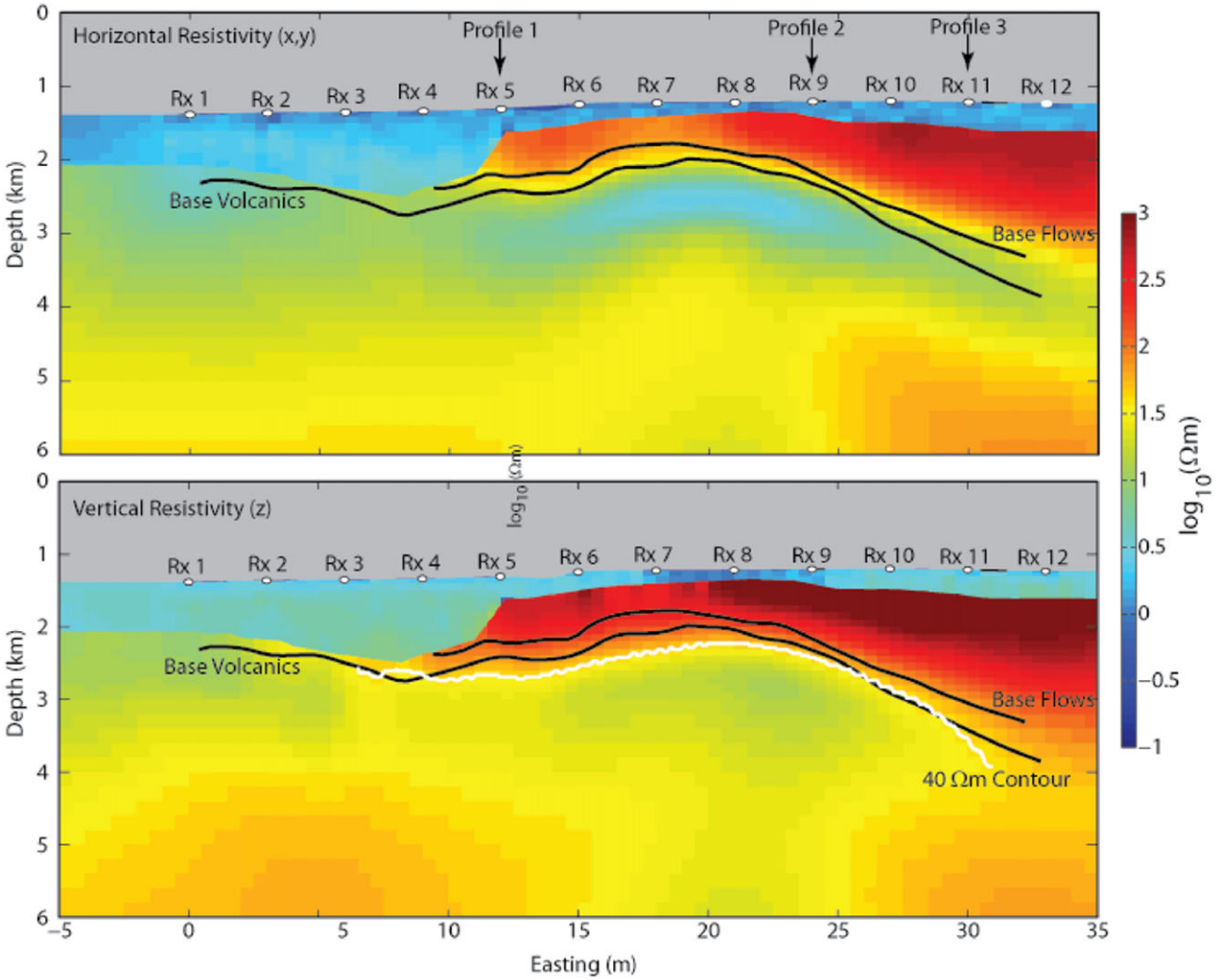

Figure 10 Model obtained from VTI inversion of CSEM-only data showing the horizontal (top) and vertical (bottom) resistivity. The starting model was 2 Ω·m from the seafloor to top of the volcanics and 100 Ω·m below the top volcanics. The base of the volcanics and base of the high resistivity flows are marked with black lines. The 40-Ω·m contour from the inversion is shown by the white line. The relative error calculations between the synthetic model and inverse model at these locations are given in Table 1.

vertical well. The comparisons are made to the macro-scale log resistivity, where the log vertical resistivity is the average over a larger interval of the measured resistivity (arithmetic mean), and the horizontal log resistivity is the inverse of the average of the log conductivity (i.e., the harmonic mean of the resistivity).

Table 2 observations are as follows.

i CSEM-only VTI inversion provides the most accurate basalt section resistance.

ii The basalt section resistance is more accurately recovered at Rosebank where the section is thinner compared with Brugdan.

iii CSEM-only VTI inversion provides the best sub-basalt section conductance at Rosebank, and CSEM and MT triaxial inversion provides the best sub-basalt section conductance at Brugdan, although the CSEM-only VTI is a close second to the CSEM and MT triaxial inversion.

iv The conductance of the conductive sections is better resolved than the resistance of resistive sections.

v There is a clear difference in the averaged siliciclastic resistivity (Rosebank) compared with the volcaniclastic resistivity (Brugdan). This difference is accurately captured in the horizontal resistivity of all the anisotropic inversions with the CSEM and MT triaxial providing the best overall estimates.

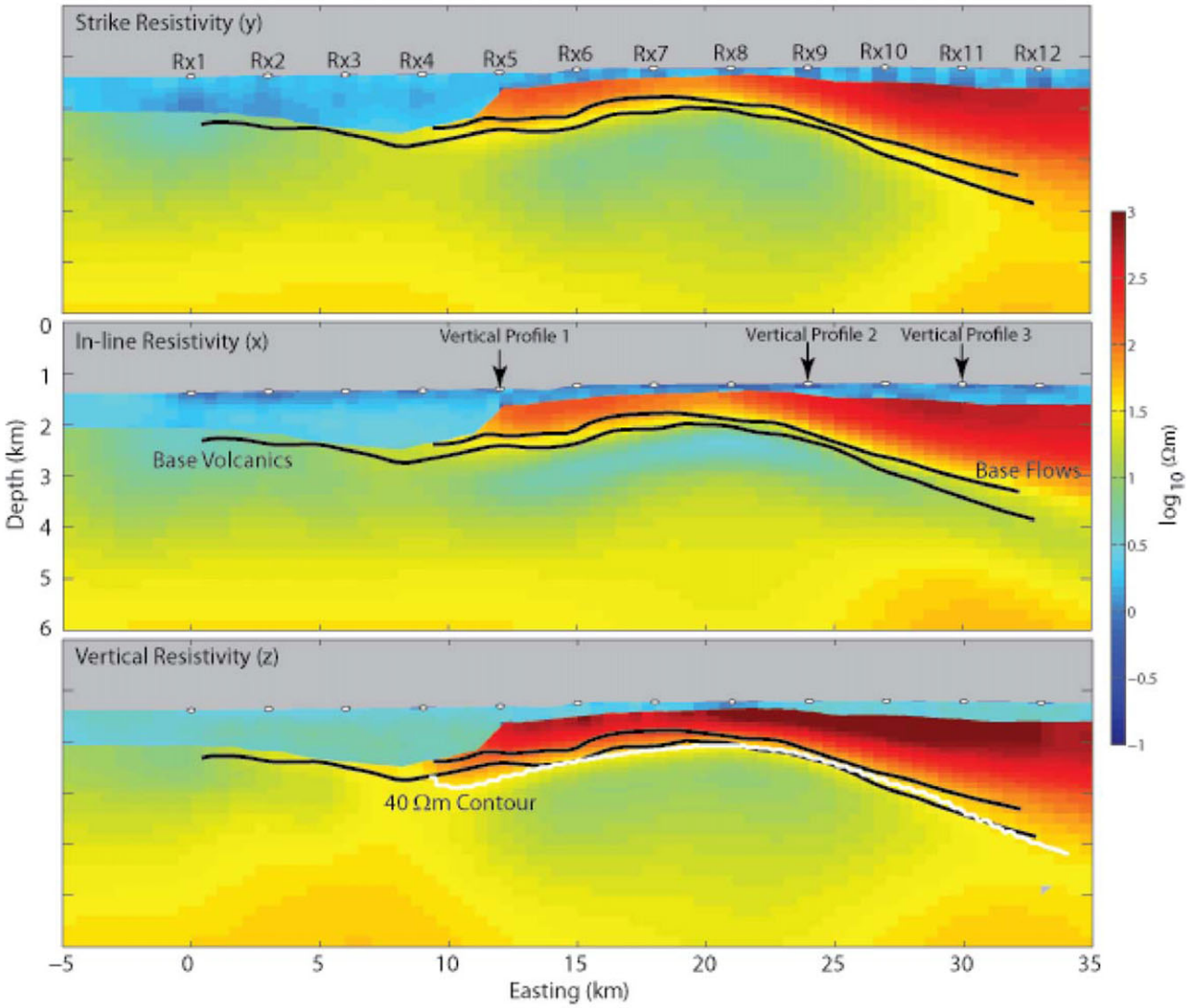

Figure 11 Model obtained from inversion for triaxial resistivity using CSEM and MT data. The starting model was 2 Ω·m from the seafloor to top of the volcanics and 100 Ω·m below the top volcanics. The base of the volcanics and base of the high resistivity flows are marked with the black line. The 40-Ω·m contour from the inversion is shown by the white line. The error in the VIR between top and base volcanics and the VIC between base volcanics and basement at the locations marked as vertical profiles 1, 2, and 3 are given in Table 1.

The difference in resistivity between volcaniclastic and siliciclastic sediments is significantly larger than the percent error in the anisotropic inversion estimates, supporting the possibility of distinguishing between the two types of sediments in anisotropic inversion.

The MT data used in all inversions shown are both TE and TM modes from 0.75 to 1350 s period. The MT impedance tensors were rotated to their maximum (averaging 23° counter-clockwise from the line direction) prior to inversion. The CSEM data used in all inversions have an SNR floor of 4:1 for frequencies of 0.2 Hz, 0.4 Hz, 0.6 Hz, 1.4 Hz, and 2.6 Hz. Just as in the inversion of the synthetic data in the feasibility section, the inversion fits the log10 of MT apparent resistivity and CSEM amplitude, and the unwrapped phase in degrees. The model resistivity values are always bounded between 0.5 Ω·m and 1000 Ω·m. The starting model for all field data inversions was 1 Ω·m below the seafloor with smoothing removed across the top volcanics, as defined by a picked seismic event. The MT-only inversion shown in Fig. 13 has a final RMS data misfit of 1.5. Other MT inversions were run with a starting model of 1 Ω·m above and 100 Ω·m below the top basalt pick; however, these inversions only differed from the

Table 2 Percentage error in basalt section resistance, percentage error in sub-basalt section conductance, sub-basalt resistivity, and percentage error in sub-basalt resistivity for the Brugdan and Rosebank wells compared with the four inversions that use CSEM data. The four inversions are: CSEM-only Isotropic (Fig. 14), CSEM VTI (Fig. 16), CSEM and MT VTI (Fig. 20), and CSEM and MT triaxial (Fig. 22). The volcanic section at the Rosebank well is 2572 m–2911 m, and at Brugdan, it is 1173 m–3175 m. The sub-basalt sediment section at Rosebank is 2911–3400 m, and at Brugdan, it is 3175–3745 m. For the joint triaxial inversion, the dip-oriented resistivity is used as it is closest to the log values. Percentage error is defined as ((well-inverse)/well)*100.

		CSEM only		CSEM & MT	
Well	Log Averaged Values	Isotropic	VTI	VTI	Triaxial
		% Error in Inversion Basalt Resistance			
Rosebank	28355 (ρt)	64.73	−26.62	41.91	56.82
Brugdan	154401 (ρt)	80.26	78.50	81.90	80.52
		% Error in Inversion Sub-basalt Concuctance			
Rosebank	20.3 (σt)	83.84	3.24	10.04	−19.16
Brugdan	43.1 (σt)	−44.12	22.80	38.56	−14.20
		Inversion Sub-basalt Resistivity			
Rosebank	3.9 (Ωm)	24.13	4.03	4.33	3.27
Brugdan	19.1 (Ωm)	13.23	24.71	31.05	16.70
		% Error in Inversion Sub-basalt Resistivity			
Rosebank	3.9 (Ωm)	−518.81	−3.35	−11.17	16.08
Brugdan	19.1 (Ωm)	30.61	−29.53	−62.77	12.44

one shown in Fig. 13 below 70 km where we have no control. In general, we have found the inversion algorithm to be quite robust with respect to the starting model, with the difference between half–space and basalt flood starting models minimal in the upper 10 km.

The MT–only inversion (Fig. 13) shows evidence of the volcanic layer at the northwest (left) end of the line where its apparent thickness is on the order of 7 km. The lack of resolution on the near-surface volcanic section near the middle of the profile is likely due to the insensitivity of MT to thin resistors, as well as the lack of high-frequency data in the deepest part of the trough (Morten *et al.* 2011). East of about –100 km the top basalt is coincident with a rise in resistivity, but no indication of base basalt is evident. The seismic basement pick shown in Fig. 13 is based on poorly imaged seismic events particularly on the eastern half of the line. However, the increase in resistivity near 10-km depth in the MT inversion to the east roughly coincides with the seismic basement pick. The large high resistivity structure seen from ~ –100 km eastward is associated with the continental crust. In general, the lower crust and upper mantle are expected to be resistive. Hence, it should all be resistive and bleed across the seismic Moho boundary, which is estimated to be around 25-km depth in this area (Grad, Tiira, and ESC Working Group 2009). The 2–30 Ω·m resistivity seen at 10–30 km depth in the westernmost side of the model is therefore intriguing and likely requires some partial melt, mantle volatiles, or even a conductive layered intrusion as observed in the Vøring plateau (Myer *et al.* 2013), but further exploration of this deep MT result is beyond the scope of this work.

In contrast to the MT inversion, the CSEM–only inversion shown in Fig. 14 clearly shows the near-surface volcanic flows. This is expected given the much greater sensitivity of CSEM data to thin resistors compared with MT data. The CSEM inversion used the top basalt seismic pick to remove smoothing across this boundary.

In conductive marine environments, conventional horizontal dipole–dipole CSEM data normally do not have much sensitivity below 4–5 km beneath the mud line. However, the depth sensitivity is enhanced by the presence of the near-surface resistive volcanics, which propagate the electromagnetic energy to greater depths. Here, the CSEM–only inversion appears to be sensitive to the resistivity structure at depths of 5–6 km below mud line, as evidenced by the indications of the mini-basin centred on –85 km in Fig. 14, as well as the transition from resistive to conductive sediments just to the southeast (right) of the Corona Ridge at –30 km position. The East Faroe High under the Brugdan well and the Corona Ridge beneath the Rosebank well are indicated in the CSEM inversion.

Figure 15 shows the isotropic resistivity from Fig. 14 extracted at the locations of the Brugdan and Rosebank wells as

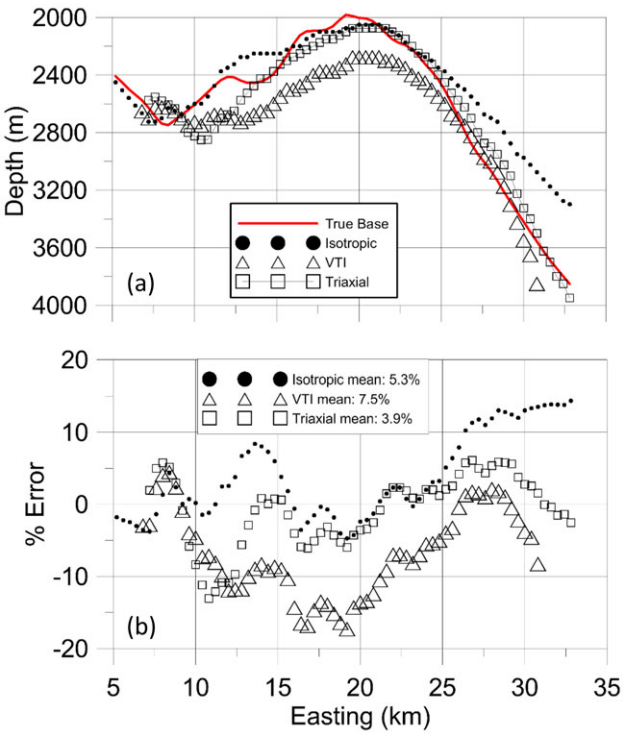

Figure 12 (a) True base volcanic depths (red line) with 40-Ω·m contour depths for isotropic CSEM-only inversion (dots), CSEM-only VTI inversion (triangles), and CSEM and MT triaxial inversion (squares). (b) Percentage error between the true and 40-Ω·m contour depths for isotropic CSEM-only inversion (dots), CSEM-only VTI inversion (triangles), and CSEM and MT triaxial inversion (squares).

solid black lines. The induction log resistivity values are shown as red dots. Because the induction log measures the horizontal resistivity in a vertical well, we have blocked the log over the major intervals and averaged the resistivity and conductivity to estimate the layer-based macro-scale vertical resistivity and horizontal resistivity, respectively. The averaged vertical resistivity and horizontal resistivity are shown as the black and green dashed lines, respectively. The vertical resistivity is the average of the resistivity values (arithmetic mean), and the horizontal resistivity is the inverse of the average of the conductivity (i.e., the harmonic mean of the resistivity).

At the Brugdan well, the base of the most resistive volcanic flows is indicated by the transition from orange (40–100 Ω·m) to light blues (~10 Ω·m) in Fig. 14 at ~3.2-km depth. Table 2 shows that the percent error in the vertical resistance is lower for the thinner section at Rosebank compared with the thicker volcanic section at Brugdan. Beneath 3.2 km, the ~13 Ω·m seen in the inversion corresponds to volcaniclastic sediments to the base of the well. In contrast to the resistivity of 13 Ω·m beneath the basalt flows at Brugdan, at Rosebank, the siliciclastic sediments encountered in the well (3–4 Ω·m) are imaged as 1–2 Ω·m at a depth of 3.5 km. In the sub-basalt sediment section, the inversion averages 24 Ω·m, which is reflected in the approximately –500% error in Table 2. The smoothing operator required to stabilize the inversion has two effects on the models, which are illustrated in Fig. 15. Sharp transitions in resistivity, such as the base of the volcanic section, are smoothed out over depth, forcing conductivity deeper

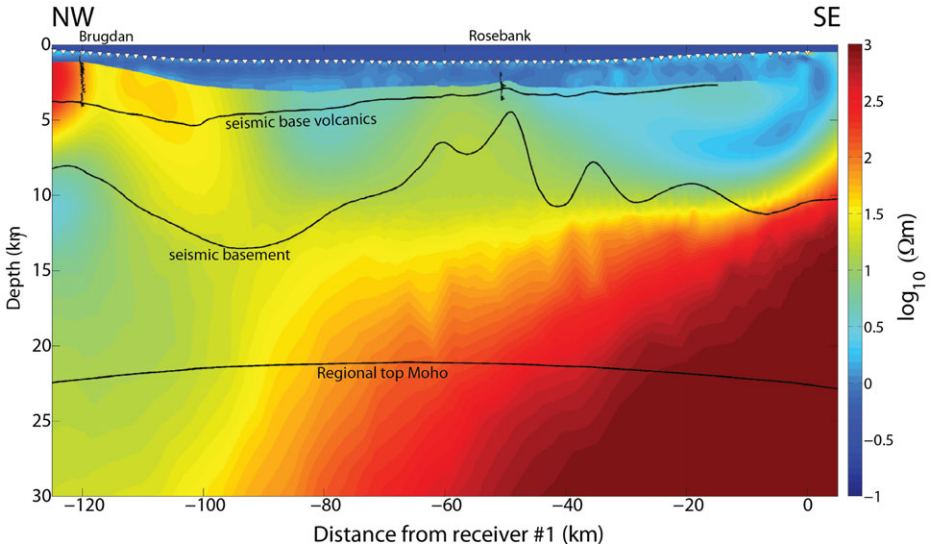

Figure 13 Isotropic inversion of TE and TM model MT data. The starting model was a 1-Ω·m half-space below the seafloor. The Brugdan and Rosebank resistivity logs are displayed for location and scale references. The volcanic section in the upper 6 km is poorly imaged.

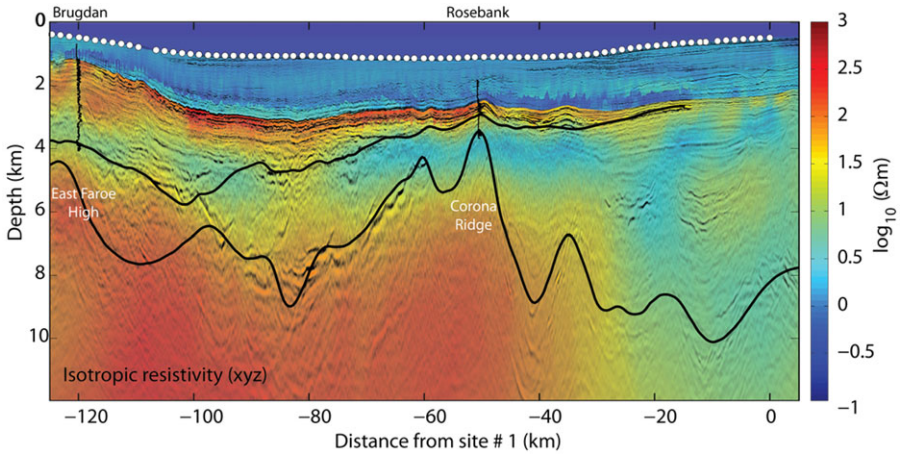

Figure 14 Inverted isotropic resistivity using CSEM data only. The starting model was a 1-Ω·m half-space below the seafloor. The overlaid seismic data are from a merge of the two 2D lines whose locations are shown in Fig. 1. The seismic line has a maximum deviation from the CSEM line of ~10 km to the south at –95 km from site #1. The Brugdan and Rosebank induction resistivity logs are overlaid. The base volcanic (upper thick black line) and top Jurassic (lower thick black line) interpreted from interpolated 2D seismic lines are overlaid for reference to the resistivity structure.

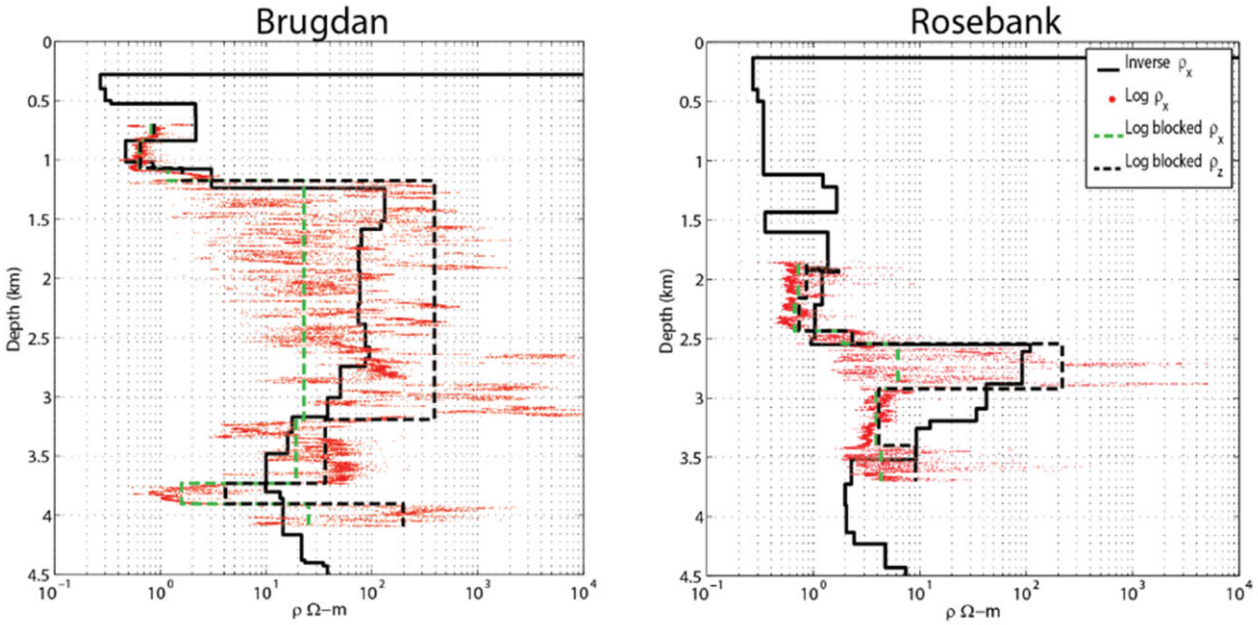

Figure 15 Extracted isotropic resistivity (solid black line) from the CSEM only inversion shown in Fig. 14. The induction resistivity logs are averaged for macro-scale horizontal (dashed green) and vertical (dashed black) resistivity for comparison.

than it should be, particularly at Rosebank where the resistivity contrast at the base of the volcanic flows is higher than at Brugdan. The second effect is that the inversion resistivity at Rosebank undershoots beneath the high-resistivity volcanic section producing the 1–2 Ω·m at depth.

Figure 16 shows the VTI inversion of CSEM–only data with the extracted resistivity and the blocked well logs shown in Fig. 17. The upper ~500 m of the volcanic section is highly anisotropic with high vertical and lower horizontal resistivity along the entire section. This area of high anisotropy in the inversion corresponds with the highest amplitude seismic reflections. At Brugdan (Fig. 17 left panel), we see the inversion underestimates both the vertical resistivity and horizontal resistivity when compared with the blocked logs in the upper

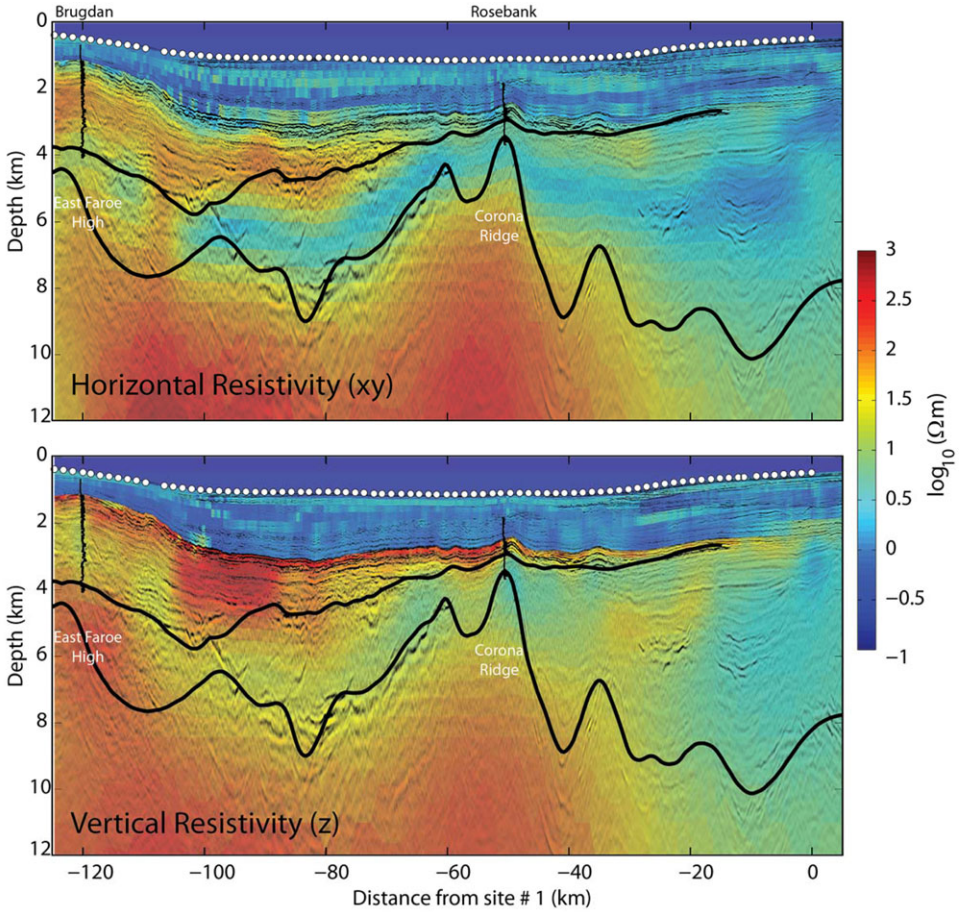

Figure 16 Inverted VTI resistivity using CSEM data only. The starting model was a 1-Ω·m half-space below the seafloor. The overlaid seismic data are from a merge of the two 2D lines whose location is shown in Fig. 1. The seismic has a maximum deviation from the CSEM line of ~10 km to the south at –95 km from site #1. The Brugdan and Rosebank induction resistivity logs are overlaid. The base volcanic (upper thick black line) and top Jurassic (lower thick black line) interpreted from interpolated 2D seismic lines are overlaid for reference to the resistivity structure.

500 m, whereas the inverted horizontal resistivity and vertical resistivity become lower toward the base of the volcanic section approaching the blocked log horizontal resistivity. Conversely, the isotropic resistivity at Brugdan (Fig. 15 left panel) lies close to the average of blocked horizontal resistivity and vertical resistivity. To the east at Rosebank, where the volcanic section thins, the inverted vertical resistivity and horizontal resistivity are much closer to the blocked log vertical resistivity and horizontal resistivity. In general, all combinations of model anisotropy and data, with the exception of MT only, more accurately predict the resistivity in the thinner volcanic section at Rosebank compared with the thick section at Brugdan (see Table 2). This is consistent with the finding on the accuracy of the resistivity–thickness product in the synthetic model for the thickest portions of the volcanic section.

Beneath the volcanic section, the vertical resistivity and horizontal resistivity from the VTI inversion (Fig. 17) are closer to the blocked log resistivity compared with the isotropic resistivity (Fig. 15). The thin conductive section at ~3.7-km depth is not recovered by any of the inversions.

Figure 18 shows the amplitude and phase data fits for the isotropic inversion of CSEM data (Fig. 14) and the VTI inversion of CSEM data (Fig. 16) at site 84, the shallow site shown in Fig. 2. Visual comparison of the data fits at this site, as at any other sites, does not reveal any significant differences. A more diagnostic display is to plot histograms of the value of the data misfits, observed minus calculated divided (normalized) by the data standard deviations. The normalized data misfit histograms for all the data used in the isotropic CSEM data inversion (Fig. 14) and the VTI CSEM data inversion (Fig. 16) are shown in Fig. 19. Figure 19 reveals a

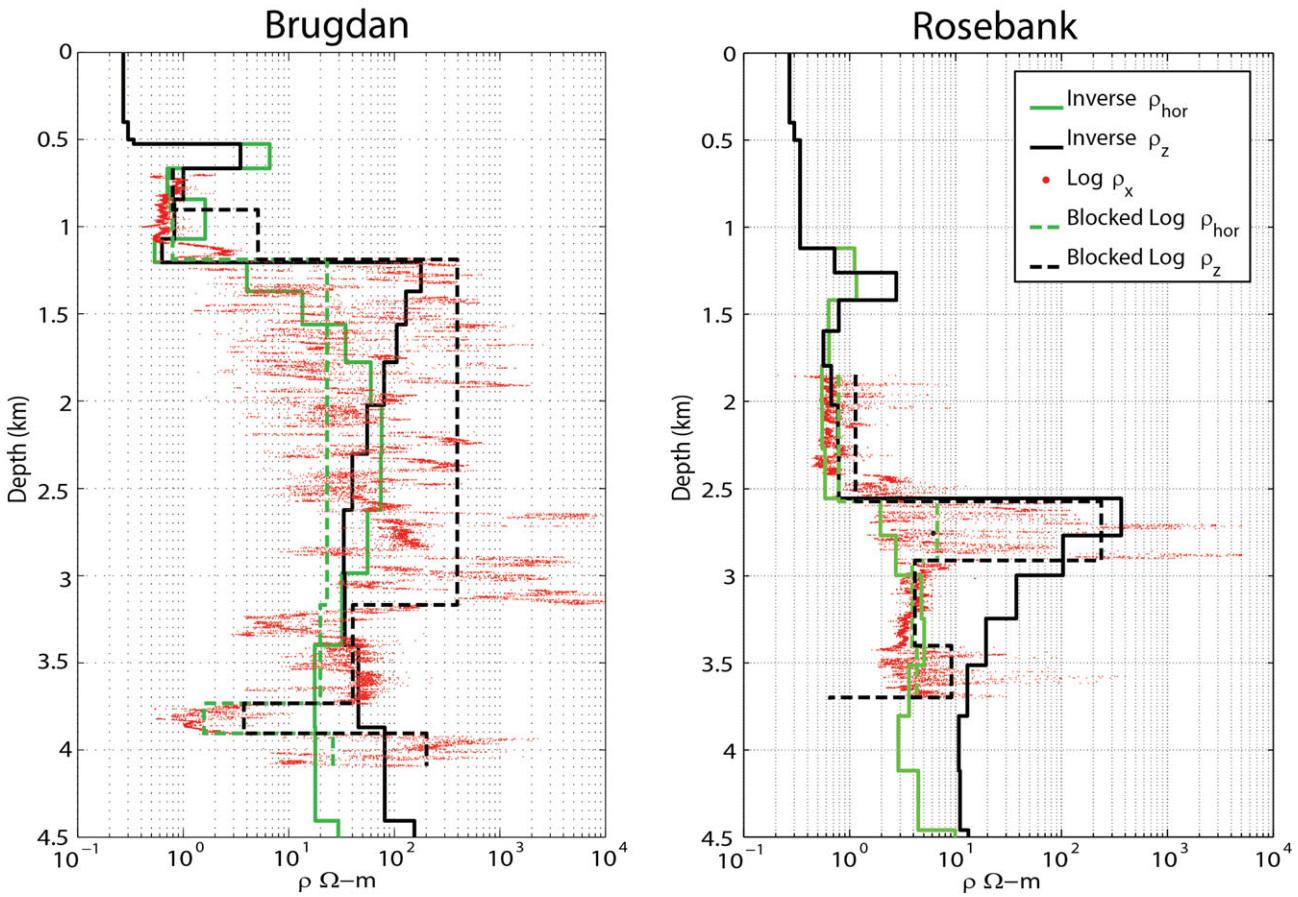

Figure 17 Extracted VTI vertical resistivity (solid black line) and horizontal (solid green line) resistivity from the CSEM-only inversion shown in Fig. 16. The induction resistivity logs are averaged for macro-scale horizontal (dashed green) and vertical (dashed black) resistivity for comparison.

subtle difference: The mean of the isotropic inversion misfits is slightly more negative than the mean of the VTI misfits (–0.11 versus –0.03). Additionally, the P_{10} and P_{90} values for the isotropic inversion show that it is more asymmetric (e.g., biased) than the VTI inversion (–1.21 to 0.9 versus–1.01 to 0.9). The differences are small but consistent with the idea that the inversion with more degrees of freedom in its model is better able to fit the observed data without bias.

Figures 20 and 21 show the VTI inversion results using both CSEM and MT data. Comparing Fig. 16 (CSEM only) with Fig. 20 (CSEM and MT) shows that the addition of the MT data has better defined the deep resistivity to the east beneath the top Jurassic seismic pick (deepest horizon pick). In addition, the mini-basin centred on –85 km is better defined as conductive sediments. The vertical resistivity from the joint inversion shows a sharper base of the resistive volcanic section at Rosebank compared with the CSEM–only inversion. In particular, note the pull down of resistivity in Fig. 16 just to the west of the Rosebank well compared with that shown in Fig. 20. At the Brugdan well, the joint inversion of Fig. 20 has produced a more uniform vertical high resistivity all the way to the bottom of the section, whereas the horizontal resistivity shows more variation from high to low within the volcanic section. The area of low resistivity centred at 4-km depth and –100 km horizontally coincides with an area that was seaward from an ancient coastline. This area shows seismic structures that are consistent with the transition from subaerial to submarine flows, producing pillow lavas and the potential for lower resistivity compared with the massive flows landward.

The 20-Ω·m contour of the vertical resistivity provides the best overall fit to the interpreted base volcanic horizon where conductive sub-volcanic sediments are present. This contour is shown as the white line in Fig. 20. The fact that the 20-Ω·m contour is closest to the interpreted base of volcanics

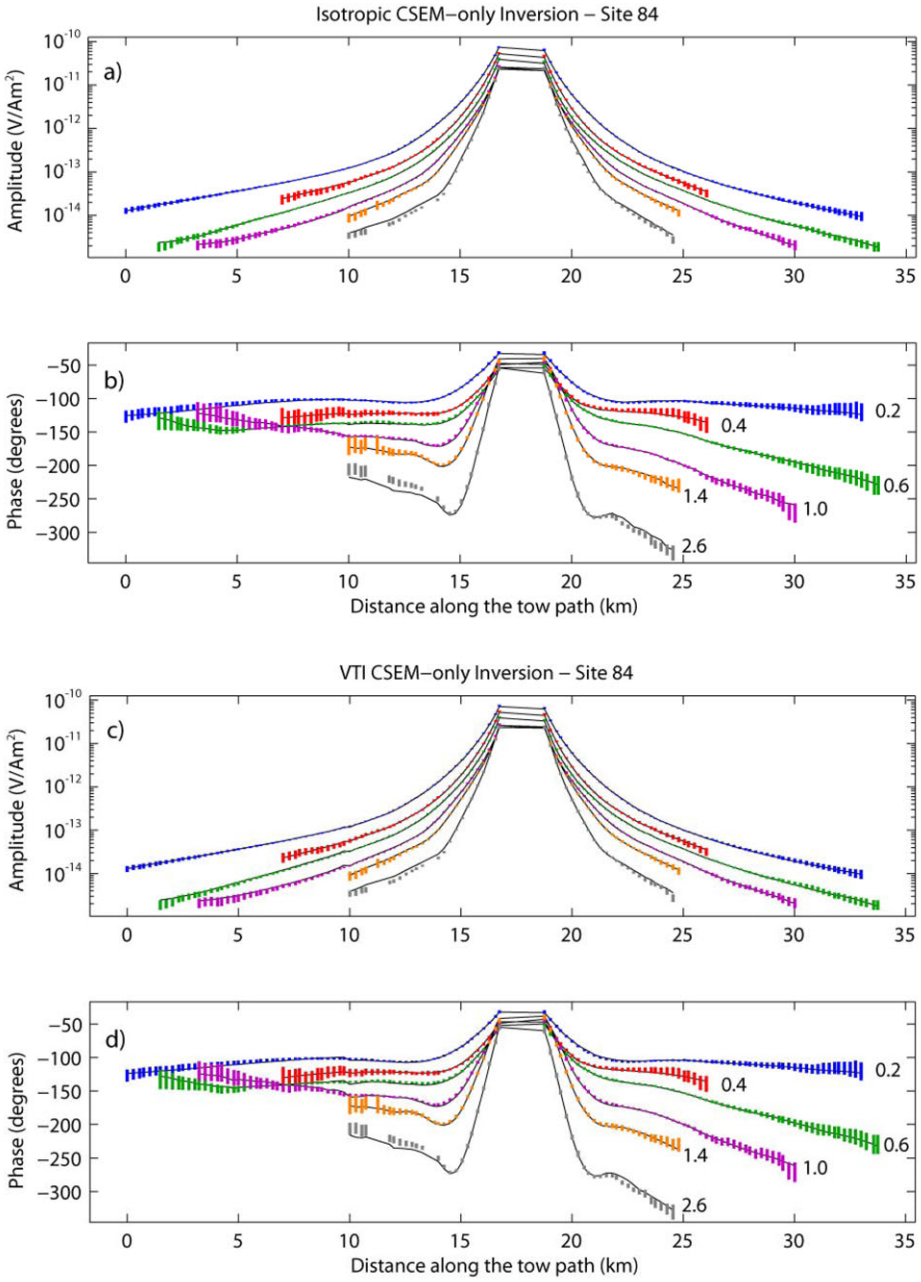

Figure 18 (a) and (b) show amplitude and phase of observed (symbols with error bars) and calculated (lines) data for site 84 from isotropic CSEM data inversion, model shown in Fig. 14. (c) and (d) show amplitude and phase of observed (symbols with error bars) and calculated (lines) data for site 84 from VTI CSEM data inversion, model shown in Fig. 16. Each color represents a frequency; frequencies are labeled on panels (b) and (d).

for the field data inversions where the 40-Ω·m contour was optimal for the synthetic model study reflects the higher volcanic resistivity of the synthetic model compared with the field study. The maximum percentage difference at any location between the 20-Ω·m contour and the interpreted base is 11% with a mean difference along the contour of 1.2%.

The inverse horizontal resistivity and vertical resistivity at the well locations (see Fig. 21) show slightly worse correlation with the averaged well resistivity compared with that

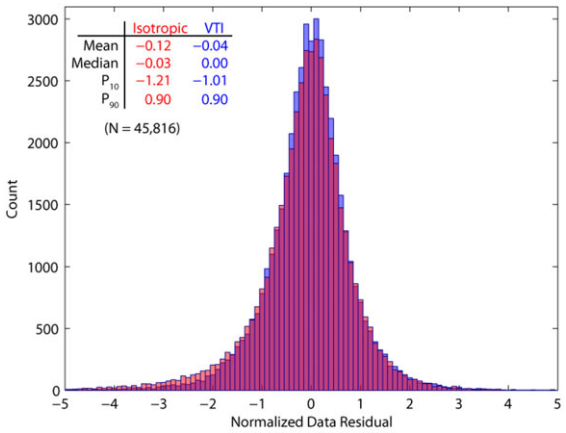

Figure 19 Histograms of the normalized data residuals for the isotropic (red) and VTI (blue) inversions along with some statistics of their distributions. The P_{10} and P_{90} values show that, although the VTI inversion is only slightly biased, the isotropic inversion is more so. Unbiased residuals should have a mean of zero and symmetrical P_{10} and P_{90} values. N is the total number of data. The isotropic inversion model is shown in Fig. 14; the VTI inversion in Fig. 16.

produced by the VTI CSEM-only inversion shown in Fig. 16, with the thinner volcanic section at Rosebank more accurately imaged than the thicker Brugdan section (see Table 2 for numerical comparison).

Finally, Figs. 22 and 23 show the results from triaxial inversion of joint CSEM and MT data. The spatial variation in the triaxial resistivity shown in Fig. 22 is much larger than in any of the lower dimensional inversions. The vertical resistivity does not have a sharp resistivity contrast at the expected base of the volcanic (the interpreted base volcanic being the shallowest black line). The fits to the logs in the basalt section are worse than the VTI inversions of either CSEM-only or CSEM and MT data. However, the fits to the logs in the sub-basalt sediments are the best of any of the inversions (see Table 2). The in-line (x) resistivity shows two near vertical high resistivity structures: one just to the east of the East Fareo High and the other centred on the Corona Ridge. It is tempting to interpret these as the core of granitic intrusions, but given the poor correlations of the models to the logs in the resistive section, this cannot be supported. These structures have less resistive expressions in the vertical resistivity. The Corona Ridge appears to have significant horizontal resistivity anisotropy, with a broad resistivity high in the Strike (y) resistivity and a much narrower vertical feature in the in-line (x) resistivity.

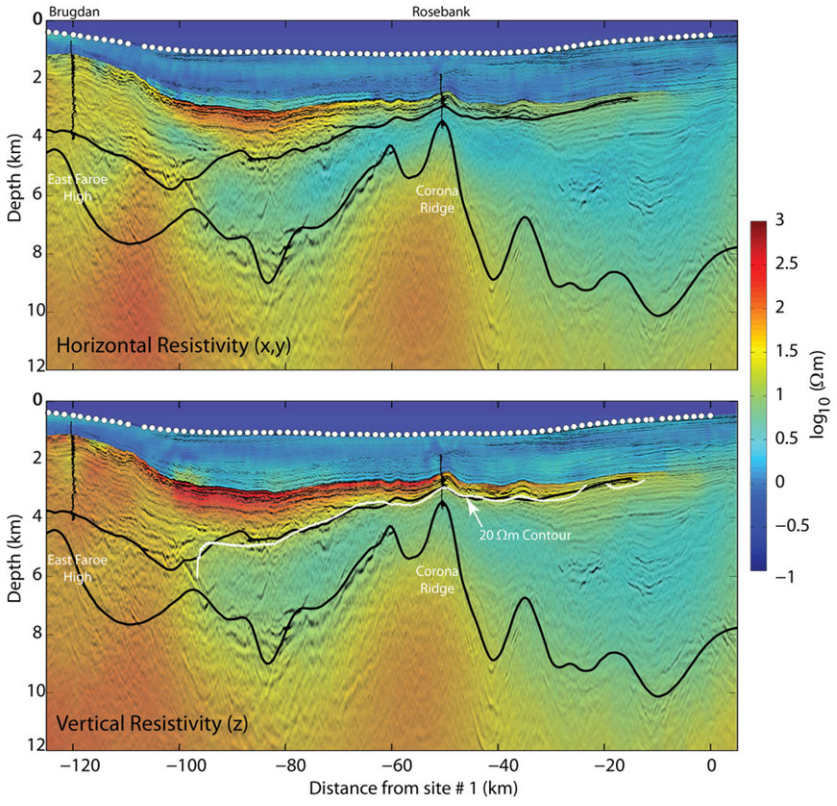

Figure 20 Inverted VTI resistivity using CSEM and MT data. The starting model was a 1-Ω·m half-space below the seafloor. The overlaid seismic data are from a merge of the two 2D lines whose location is shown in Fig. 1. The seismic has a maximum deviation from the CSEM line of ~10 km to the south at –95km from site #1. The Brugdan and Rosebank induction resistivity logs are overlaid. The base volcanic (first black line from the top) and top Jurassic (deep black line) interpreted from interpolated 2D seismic lines are overlaid for reference to the resistivity structure. The 20-Ω·m contour from the vertical resistivity is overlaid on the vertical resistivity section as a white line. Note that the high correlation between the interpreted base of the volcanic section and the 20-Ω·m contour.

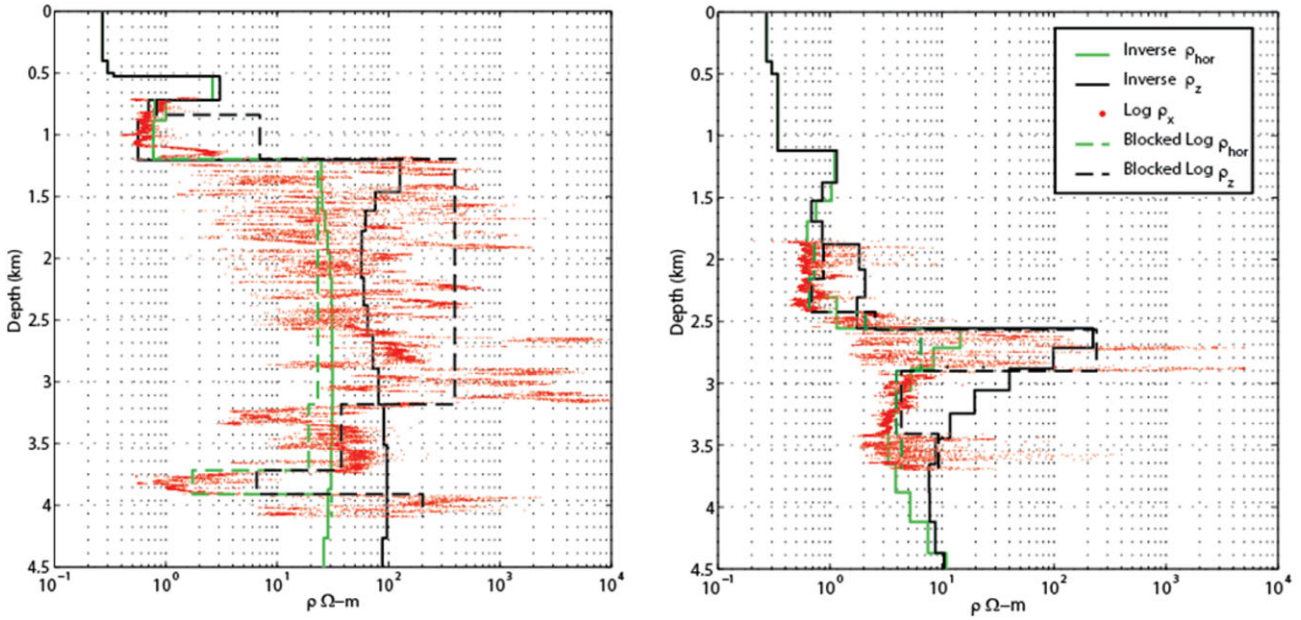

Figure 21 Extracted VTI vertical resistivity (solid black line) and horizontal (solid green line) resistivity from the joint CSEM and MT data inversion shown in Fig. 20. The induction resistivity logs are averaged for macro-scale horizontal (dashed green) and vertical (dashed black) resistivity for comparison.

The closest resistivity contour in the vertical resistivity is 40 Ω·m and is shown as the white line on the bottom panel of Fig. 22. The contour highlights the pull down in vertical resistivity just to the west of the Rosebank well compared with the interpreted base volcanic (black line). The maximum relative difference at any location between the 40-Ω·m contour and the interpreted base is 22% with a mean difference along the contour of 5.1%.

DISCUSSION

The synthetic model study found that the joint controlled source electromagnetic (CSEM) and marine magnetotelluric (MT) inversion for vertical transverse anisotropy (VTI) resistivity produced better VIR predictions in the volcanic section with CSEM-only VTI inversion producing slightly better VIC predictions in the underlying sediments. The joint inversion of field data with VTI inversion produces closer matches to the blocked logs and a vertical resistivity contour that more closely follows the interpreted base volcanic horizon. However, in the field data, the CSEM and MT data VTI inversion was superior to the CSEM–only VTI inversion for matching the base of the interpreted volcanic flows. The field data triaxial inversions are worse for predicting basalt thickness than suggested by the feasibility study for triaxial inversion. However, the triaxial joint inversion does produce slightly better sub-basalt horizontal resistivity estimated compared with VTI joint inversion, but the improvement is small and may not be robust due to the increase in degrees of freedom for triaxial compared to VTI. Overall, the sensitivity results seen in the feasibility study are borne out in the field data examples. Using only inline E field data limits the model parameterization to VTI. We speculate that, in the synthetic model data, which has primarily Gaussian noise, the sensitivity to the strike resistivity (y) is higher than in the field data where noise is not completely Gaussian and 3D effects are higher. The synthetic model did not include complex dike and sill structures that are most likely in the real geology. Therefore, in the more complex 3D geology seen by the field data, the in-line CSEM data has less sensitivity to the strike resistivity than suggested in the synthetic study. Additionally, the 3D MT affects in the field data are most likely larger than in the synthetic model study, adding more uncertainty when trying to invert for triaxial resistivity on a single 2D line.

The apparent ability to discriminate between 10-Ω·m volcaniclastic and 3–4 Ω·m siliciclastic sediments in the CSEM field data inversions was an unexpected result. While more data and well control will be needed to substantiate the ability to discriminate between volcaniclastic and siliciclastic sediments, if true, this capability would significantly enhance the value of electromagnetic surveys in sub-volcanic provinces.

The apparent ability of the joint CSEM and MT VTI inversions to produce vertical resistivity where there is a high correlation between a constant resistivity contour (20 Ω·m in

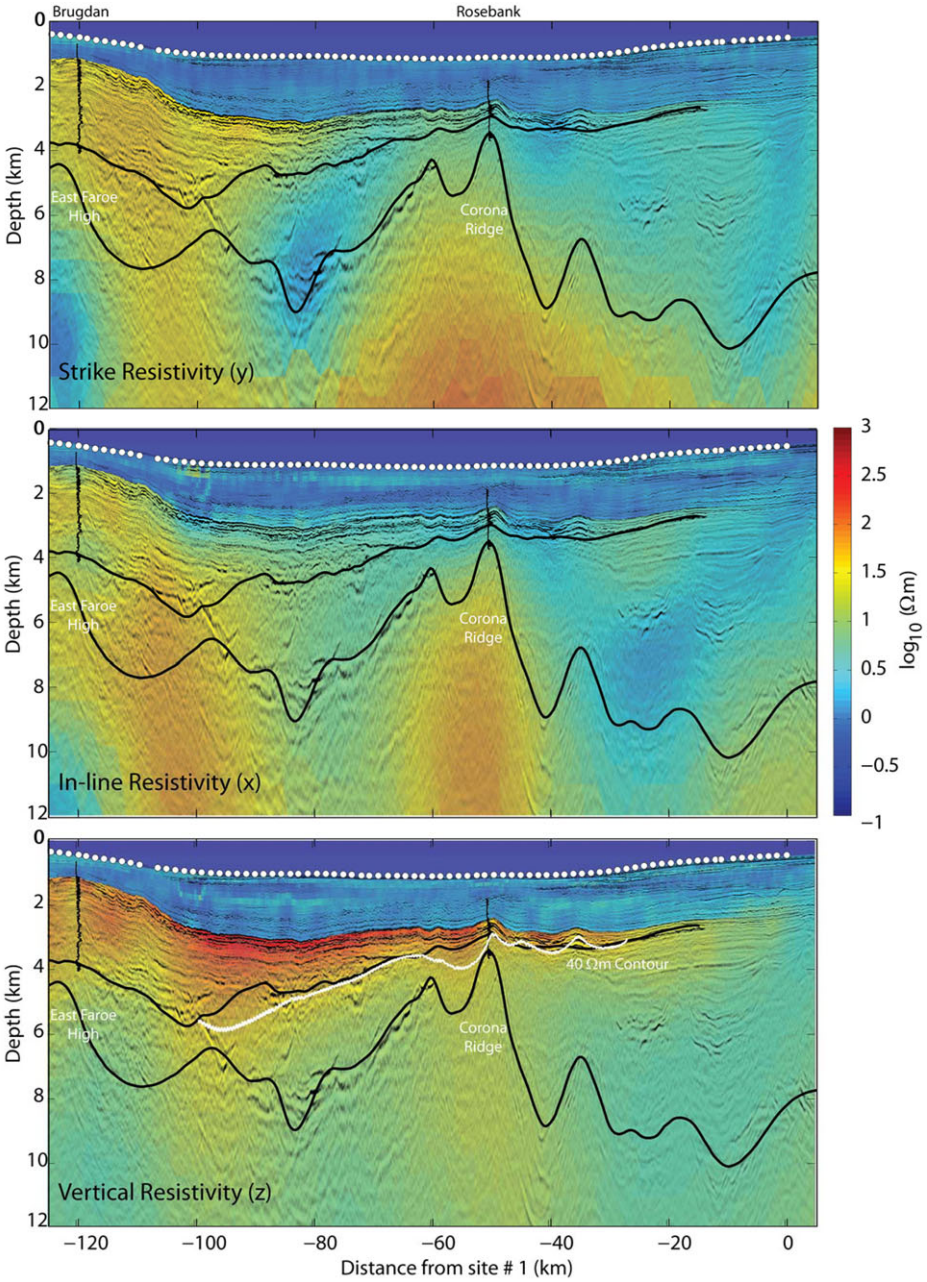

Figure 22 Inverted triaxial resistivity using CSEM and MT data. The starting model was 1 Ω·m below the seafloor. The overlaid seismic data are from a merge of the two 2D lines whose location is shown in Fig. 1. The seismic has a maximum deviation from the CSEM line of ~10 km to the south at –95 km from site #1. The Brugdan and Rosebank induction resistivity logs are overlaid. The base volcanic (upper thick black line) and top Jurassic (lower thick black line) interpreted from interpolated 2D seismic lines are overlaid for reference to the resistivity structure. The 20-Ω·m contour from the vertical resistivity is overlaid on the vertical resistivity section as a white line.

this case) and the base of the high-velocity volcanic section offers new information for velocity model building. Figure 24 shows the joint CSEM and MT VTI vertical resistivity section where a 20-Ω·m vertical resistivity threshold separates red from blue. This provides a quick high–low velocity model for migration testing. The best workflows to make use of the inverted resistivity in velocity model building are an area of on-going research.

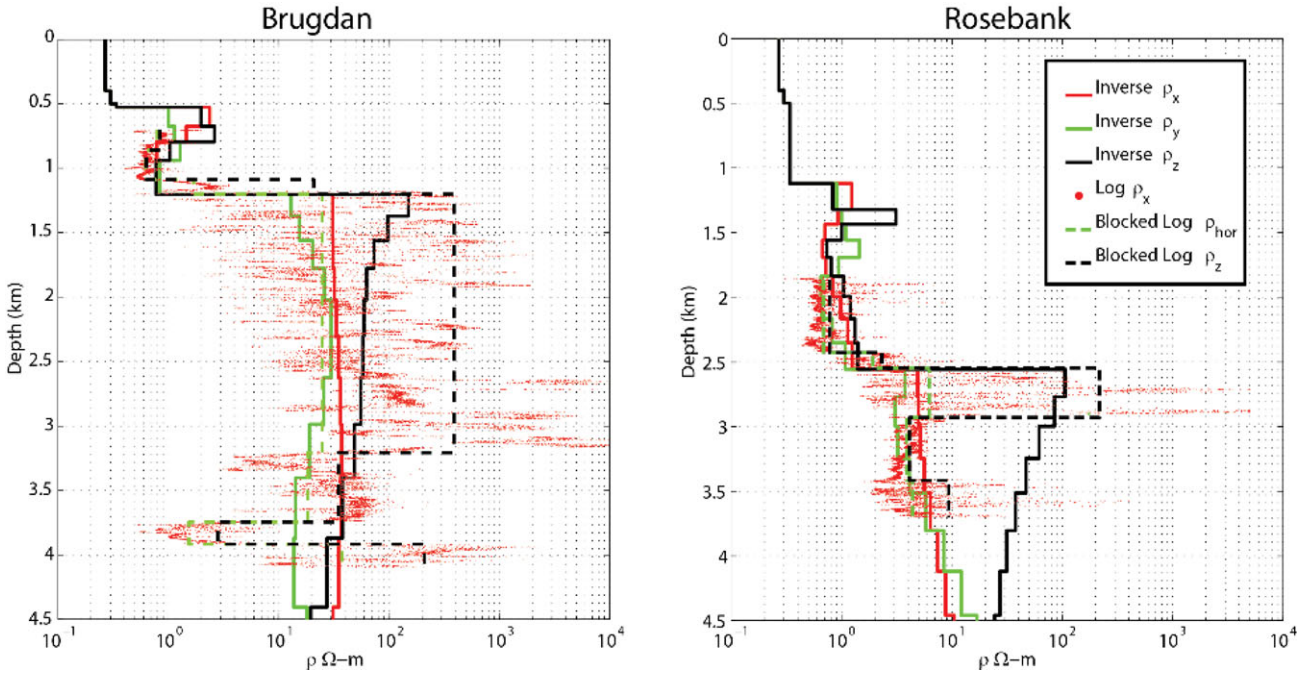

Figure 23 Extracted triaxial in-line (x) resistivity (solid red line), strike (y) resistivity (solid green line), and vertical (z) resistivity (solid black line) from joint inversion of CSEM and MT data shown in Fig. 2. The induction resistivity logs are averaged for macro-scale horizontal (dashed green) and vertical (dashed black) resistivity for comparison.

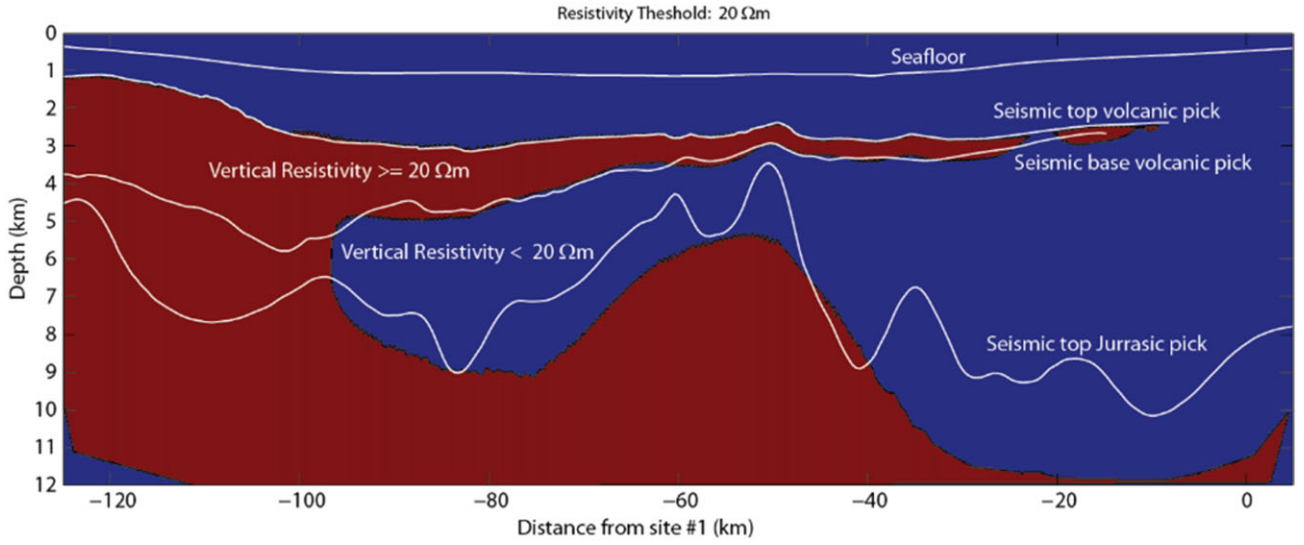

Figure 24 Red–blue plot of the vertical resistivity obtained from VTI inversion of the CSEM and MT data, shown in Fig. 20. Red is vertical resistivity > = 20 Ω·m, and blue is vertical resistivity < 20 Ω·m.

CONCLUSIONS

The CSEM and MT calibration line described here demonstrates that high-quality marine CSEM and MT data can provide significant information to reduce uncertainty in base volcanic picks and to modify seismic interpretations of the base of the volcanic section as well as sediment constraining basement depths. In addition, the resistivity images from this survey indicate the possibility of distinguishing between volcaniclastic and more conductive siliciclastic sediments. If the ability to distinguish volcaniclastic sediment from siliciclastic sediment

is borne out in further surveys, this could prove to be a significant uplift in what was previously thought of only as a base basalt mapping technology.

For both the model and field data studies, inversions that used both CSEM and TE-mode and TM-mode MT data provided the best results. The joint inversion for triaxial resistivity provided the best results for the synthetic model. However, for the field data, the best sub-basalt horizontal resistivity came from Triaxial joint inversion, whereas the vertical resistivity from VTI joint inversion provided better correlation with the interpreted base of the volcanic section. This most likely indicates that the data need to be nearly 2D to be able to distinguish three separate resistivity components from 2.5D inversion. The increased 3D effects in the volcanic flows with non-Gaussian noise in the field data produce more non-unique tradeoffs in the three resistivity components in the volcanic flows. Picking a constant contour of resistivity from the isotropic inversion or the vertical resistivity from an anisotropic inversion provided nearly identical average errors across the model with the joint inversion triaxial vertical resistivity providing the most accurate base volcanic flow. Additionally, the differences between all inversions in predicting the thickness of the volcanic flows at Rosebank (where we have a full volcanic section penetration) using the field data indicates that isotropic inversion may often be adequate. While VTI 2.5D inversion of field data may provide better resolution of thicknesses and resistivities, it should be tested against models on a case-by-case basis.

ACKNOWLEDGEMENTS

The CSEM survey was acquired by EMGS. The authors would like to thank Chevron Europe and EMGS for permission to publish this work. K. Key acknowledges support from the Scripps Seafloor Electromagnetic Methods Consortium.

REFERENCES

Alumbaugh D., Hoversten M., Stefani J. and Thacher C. 2013. A 3D model study to investigate EM imaging of sub-basalt structures in a deep water environment. 83rd SEG meeting, Houston, USA, Expanded Abstracts, 765–769.

Colombo D., Keho T., Janoubi E. and Soyer W. 2011. Sub-basalt imaging with broadband magnetotellurics in NW Saudi Arabia. 81st SEG annual meeting, San Antonio, USA, 619–623.

Commer M. and Newman G.A. 2009. Three-dimensional controlled-source electromagnetic and magnetotellurics joint inversion. *Geophysical Journal International* **178**, 1305–1616.

Connell D. and Key K. 2013. A numerical comparison of time and frequency-domain marine electromagnetic methods for hydrocarbon exploration in shallow water. *Geophysical Prospecting* **61**, 187–199.

Constable S., Weiss C.J. 2006. Mapping thin resistors and hydrocarbons with marine EM methods: Insights from 1D modeling. *Geophysics* **71**, G43–G51.

Constable S.C., Orange A., Hoversten G.M. and Morrison H.F. 1998. Marine magnetotellurics for petroleum exploration, Part 1: A seafloor equipment system. *Geophysics* **63**, 816–825.

Egbert G.D. 1997. Robust multiple-station magnetotelluric data processing. *Geophysical Journal International* **130**(2), 475–496.

Ellis M. and MacGregor L. 2012. An electrical rock physics model for partially interconnected fluid inclusions/cracks. 82nd SEG annual meeting, Las Vegas, USA, Expanded Abstracts, 1–5.

Grad M., Tiira T. and ESC Working Group 2009. The Moho depth map of the European Plate. *Geophysical Journal International* **176**, 279–292.

Hoversten G.M., Morrison H.F. and Constable S.C. 1998. Marine magnetotellurics for petroleum exploration, Part 2: Numerical analysis of subsalt resolution. *Geophysics* **63**, 826–840.

Jegen M.D., Hobbs R.W., Tarits P. and Chave A. 2009. Joint inversion of marine magnetotelluric and gravity data incorporating seismic constraints Preliminary results of sub-basalt imaging off the Faroe Shelf. *Earth and Planetary Science Letters* **282**(1–4), 47–55.

Key K.W., Constable S.C. and Weiss C.J. 2006. Mapping 3D salt using the 2D marine magnetotelluric method: Case study from Gemini Prospect, Gulf of Mexico. *Geophysics* **71**(1), B17–B27.

Key K. and Lockwood A. 2010. Determining the orientation of marine CSEM receivers using orthogonal Procrustes rotation analysis. *Geophysics* **75**(3), F63–F70.

Key K. and Ovall J. 2011. A parallel goal-oriented adaptive finite element method for 2.5-D electromagnetic modeling. *Geophysical Journal International* **186**(1), 137–154.

Key K. 2012. Marine EM inversion using unstructured grids: a 2D parallel adaptive finite element algorithm. 82nd SEG annual meeting, Las Vegas, USA, Expanded Abstracts 1–5.

Klein J.D., Martin P.R. and Allen D.F. 1997. The petrophysics of electrically anisotropic reservoirs. *The Log Analyst* **38**, 25–36.

Morten J.P., Fanavoll S. and Mrope F.M. 2001. Sub-basalt Imaging Using Broadside CSEM. *73rd EAGE Conference and Exhibition*, C029.

Morrison H.F., Shoham Y., Hoversten G.M. and Torres-Verdin C. 1996. Electromagnetic mapping of electrical conductivity beneath the Columbia basalts. *Geophysical Prospecting* **44**, 963–986.

Myer D., Constable S. and Key K. 2011. Broad-band waveforms and robust processing for marine CSEM surveys. *Geophysical Journal International* **184**(2), 689–698.

Myer D., Constable S. and Key K. 2013. Magnetotelluric evidence for layered mafic intrusions beneath the Vøring and Exmouth rifted margins. *Physics of the Earth and Planetary Interiors* **220**, 1–10.

Newman G.A., Commer M. and Carazzone J.J. 2010. Imaging CSEM data in the presence of electrical anisotropy. *Geophysics* **75**, F51–F61.

Smith T., Hoversten G.M., Gasperikova E. and Morrison F. 1999. Sharp boundary inversion of 2D magnetotellurics data. *Geophysical Prospecting* **47**, 469–486.

Strack K.M. and Pandey P.B. 2007. Exploration with controlled-source electromagnetic under basalt cover in India. *The Leading Edge* **26**, 260–363.

Warren R.K. and Srnka L.J. 1992. Exploration in the basalt-covered areas of the Columbia River Basin, Washington, using electromagnetic array profiling (EMAP). *Geophysics* **57**, 986–993.

Weckmann U., Magunia A. and Ritter O. 2005. Effective noise separation for magnetotelluric single site data processing using a frequency domain selection scheme. *Geophysical Journal International* **161**(3), 635–652.

Withers R., Eggers D., Fox T. and Crebs T. 1994. A case study of integrated hydrocarbon exploration through basalt. *Geophysics* **59**, 666–1679.